We are IntechOpen, the world's leading publisher of Open Access books Built by scientists, for scientists

4,800
Open access books available

122,000
International authors and editors

135M
Downloads

Our authors are among the

154
Countries delivered to

TOP 1%
most cited scientists

12.2%
Contributors from top 500 universities

WEB OF SCIENCE™

Selection of our books indexed in the Book Citation Index
in Web of Science™ Core Collection (BKCI)

Interested in publishing with us?
Contact book.department@intechopen.com

Phase Equilibrium Evolution in Single-Crystal Ni-Based Superalloys

Lembit Kommel

Additional information is available at the end of the chapter

Abstract

The phase equilibrium evolution resulting from the interdiffusion of atoms in single crystals of nickel-based superalloys was studied with the aid of microstructural, chemical composition, and micromechanical property investigations. The experimental observation methods—optical microscopy, scanning electron microscopy, transmission electron microscopy, energy-dispersive spectroscopy, microchemical analyses, X-ray diffraction, hard cyclic viscoplastic deformation, and nanoindentation—were combined to obtain new insights into the phases' chemical composition and micromechanical properties' characterization that depend on strain-stress levels which are induced by tension-compression cycling in viscoplastic conditions at room temperature. The test samples with differences in the strain-stress parameters were received on the tension-compression stepped sample with four different cross-section areas. The strains with four levels of intensivity were added by using strain amplitudes of 0%–0.05%, 0%–0.2%, 0%–0.5%, and 0%–1% for 30 cycles, respectively. Microstructural investigations show that dendrite length decreased significantly in samples with minimal cross-section and accordingly at maximal strain-stress amplitudes. The main dendrites of the (001) direction were separated by $(\gamma + \gamma')$-eutectic pools. The length of newly formed dendrites depends on cumulative strain-stress amplitudes. The chemical composition and micromechanical properties of phases were changed as a result of the atoms' interdiffusion between different phases. These changes were influenced on the phases' equilibrium evolution of the single-crystal superalloy during testing.

Keywords: phase equilibrium, evolution, nickel-based superalloys, atom interdiffusion

1. Introduction

Cast single-crystalline (SC) Ni-based superalloys are promising high-strength refractory materials for manufacturing turbine blades (Figure 1) and vanes of turbojet engines as well as power gas turbine blades and polycrystalline turbine discs.

Channels for air cooling

Figure 1. Air-cooled and thermal barrier-coated high-temperature turbine blade for turbojet engine Al31-F.

It is well-known that these materials possess extraordinary strength [1-3], high fracture toughness at fretting failure [4], good resilience under thermomechanical fatigue [5-8], low-cycle fatigue (LCF) [9], and high-cycle fatigue (HCF) [10, 11] as well as high oxidation resistance [12, 13] in gas environments at high temperatures during long-term exposures. The excellent creep-rupture lifetime properties of superalloys are presented in a large number of investigations [14-17]. These excellent exploitation properties of the superalloys depend on the chemical composition [1, 18, 19], solidification parameters [20-22], and casting conditions [23] of the manufacturing process. The dendrite microstructures of SC Ni-based superalloys differ based on their withdrawal, solidification, and cooling rates. The withdrawal rate and temperature gradient have effects on the dendritic microstructure evolution in directionally solidified SC of superalloys. The primary dendrite arm spacing for some commercial superalloys depends on the temperature gradient and withdrawal velocity, and their spacing varied from 50 to 550 μm for a number of commercial superalloys [20-22]. The withdrawal rate and melt overheating temperature, as well as cooling rate, also influence the primary dendrite length [22]. Therefore, the tensile and creep properties of these materials are not simply a function of the withdrawal rate. Usually, the withdrawal rates varied from 50 to 350 mm/h [20-22]. The primary and secondary dendrite arm spacing decreases with increasing withdrawal rate [21, 22]. The fine dendritic structure can lead to increased mechanical properties and higher solution and liquidus temperatures [21]. The cooling rate increase influences both the solidification behavior and the resultant structural and increased chemical microheterogeneity of the as-cast structure

of superalloys [23]. As a result, the creep and fatigue strengths were increased by chemical microheterogeneity increases. Therefore, the number of solidification defects, like silvers and freckles in castings, can possibly be decreased by the addition of C, B, and N [18]. Therefore, for superalloys the selection of elements is an importance. The major constituent of commonly cast superalloys is nickel (Ni) and the main alloying elements are Cr, Co, Mo, Nb, Ta, Ti, Fe, V, W, Ru, Re, Ir, Hf, B, C, and Al [1, 20]. These elements have BBC, HCP, and FCC crystal structures (Figure 2). The listed elements with atomic numbers have the highest melting temperatures (Figure 3) and the lowest normalized activation energies for diffusion (Figure 4). To provide the best exploitation properties (lowered creep, high resistance to thermomechanical fatigue, and so on) for turbine blades, the elements can have high activation energies for high-temperature creep [24, 25] and activation energy for self-diffusion [25, 26], as shown in Figure 5. Diffusion in SC Ni-based superalloys under viscoplastic deformation at room temperature is studied in [27, 28]. The elements (W, Ta, Nb, and Re) with the needed higher activation energies for self-diffusion control mass transport via diffusion on the scale of the microstructure of the superalloy. In contrast, Ti has the lowest activation energy (Figure 5) for diffusion, high-temperature creep, and is not a suitable alloying element for casting SC superalloys [28]. The Al forms high-temperature intermetallic compounds in γ'-phase with Ni as well with other alloying elements (Ti, Ta, and Nb). Metal carbides (MC) [29] are formed on the base of C, with Nb and Ta or Ti and Ta.

IIIB	IVB	VB	VIB	VIIB	←	— VIIIB —	→	IB	IIB
21 Sc 44.956	22 Ti 47.90	23 V 50.942	24 Cr 51.996	25 Mn 54.9380	26 Fe 55.847	27 Co 58.9332	28 Ni 58.71	29 Cu 63.54	30 Zn 65.37
39 Y 88.905	40 Zr 91.22	41 Nb 92.906	42 Mo 95.94	43 Tc [99]	44 Ru 101.07	45 Rh 102.905	46 Pd 106.4	47 Ag 107.870	48 Cd 112.40
✳ 57 La 138.91	72 Hf 178.49	73 Ta 180.948	74 W 183.85	75 Re 186.2	76 Os 190.2	77 Ir 192.2	78 Pt 195.09	79 Au 196.967	80 Hg 200.59

BCC   HCP   FCC   Liquid

Figure 2. Correlation of the crystal structures of the transition metals (position in the periodic table) used for SC superalloy casting. Adapted from reference [1].

It is shown that MC is beneficial for creep property improvement, but transformed to M_6C, provides micropore formation, crack initiation, and led to final fracture. Thus, the choice of temperature regime for solution/homogenization heat treatment is the key to achieving the best properties for SC cast superalloys [30]. The historical development of superalloys (during 75 years) from their emergence in the 1940s is important [1]. The turbine entry temperature (TET) was improved from 700°C (wrought, uncooled) to 1850°C (SC, cooled, thermal barrier coated) at present (Figure 1). During this period, the high-temperature capability increased as the production technology was improved from wrought to conventional casting, to directional
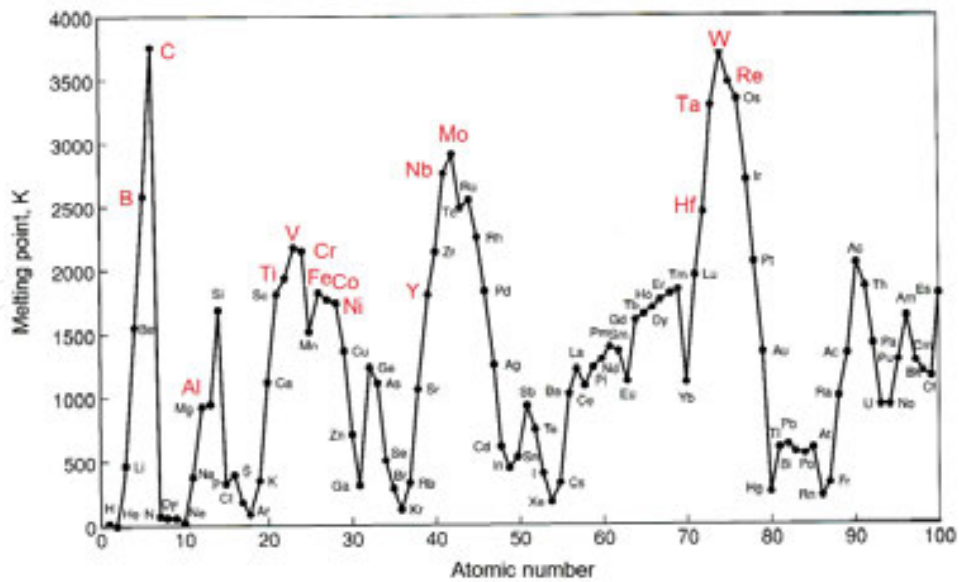
Figure 3. Alloying elements (with increased font, red-colored, mainly used for SC Ni-based superalloy casting, Fe was used for polycrystalline superalloys) melting temperatures for corresponding atomic number. Data taken from reference [1].
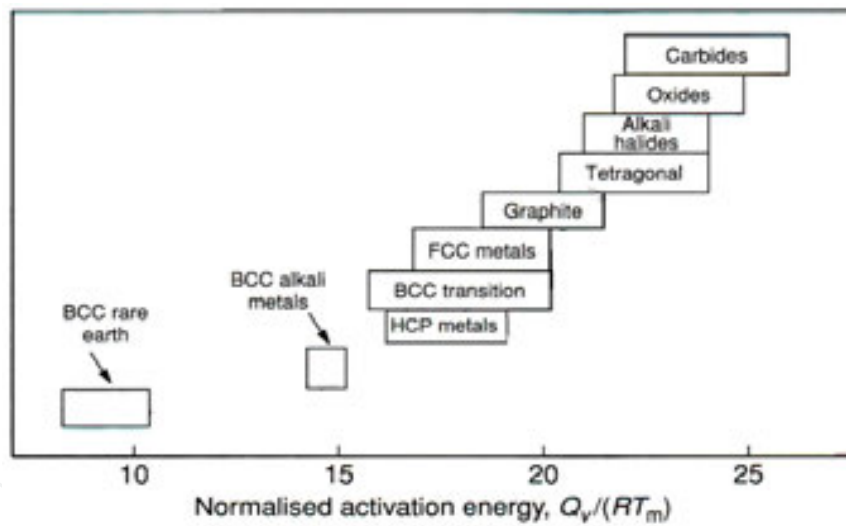

Figure 4. Normalized activation energies of diffusion for the various crystal classes. Adapted from reference [1].

solidification and then to single-crystal superalloy casting in directional solidification installation under high vacuum [20-23, 28-30].

2. Review of conventional high-temperature test methods

During exploitation, the gas turbines experience different temperature cycles and the turbine-entered temperature (TET) varies from ±60°C at ground idle during relative short time [1] up
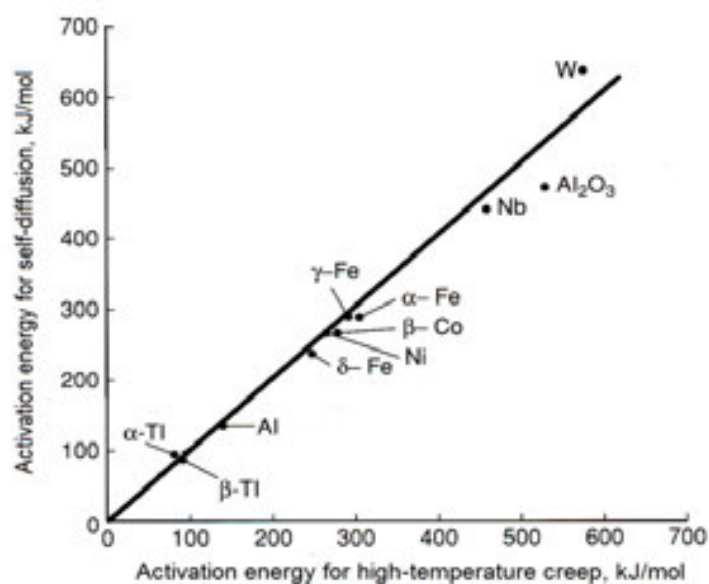
Figure 5. Correlation between the high-temperature creep activation energy and the activation energy for self-diffusion for several elements. Adapted from reference [1].

to 1850ºC during the take-off and climb to cruising altitude during a typical flight cycle. According to the turbine blade and disc materials, with single crystalline and polycrystalline microstructures, respectively, mainly are studied at high temperatures. The high-temperature creep [31-33] and metallurgical failure [34] of turbojet turbine rotor blade materials under mechanical tension, vibration, buffeting, and thermal tension-compression loadings at centrifugal forces during rotation are some of the most important problems in aircraft engines. Gas turbine rotor blades generally experience thermomechanical fatigue [6, 7] as well stresses at different locations in the turbine blade body under loadings in gaseous surroundings at high temperatures. Under low cycle fatigue (LCF) testing conditions at strain control regimes, the fatigue performance depends on the loading axis direction to crystal orientation (Figure 6). The yield stress at tension is maximal for the (001) direction of crystal orientation. The yield stress in tension depends on the temperature and exceeds that of compression. The strain softening of materials increase as temperatures increase. Determining all these influences during the viability testing of a blade material is complicated. Therefore, the test method that is currently used to determine the mechanical properties of Ni-based superalloys is creep testing at elevated temperatures and during very long (100-1000 h) exposure times [14-17, 31-33]. The high-temperature creep testing of superalloys is typically performed at 800°C-1100°C under tension load of 600-200 MPa, respectively. Usually, increased temperatures used lowered tension stresses. The microstructural aspects of high-temperature deformation of mono- or single crystalline nickel-based superalloys are well studied by Mughrabi [31]. The resulting creep dislocations help to form a raft structure (Figure 7), which is elastically unstable. The rafts forming direction depends on the stresses in PDA or SDA of dendrites and the orientations of rafts are "N" or "P" type (Figure 8). Thus, the rafts' orientation also depends on various γ' volume fractions.

forming direction depends on the stresses in PDA or SDA of dendrites and the orientations of rafts are "N" or "P" type (Figure 8). Thus, the rafts' orientation also depends on various γ' volume fractions.
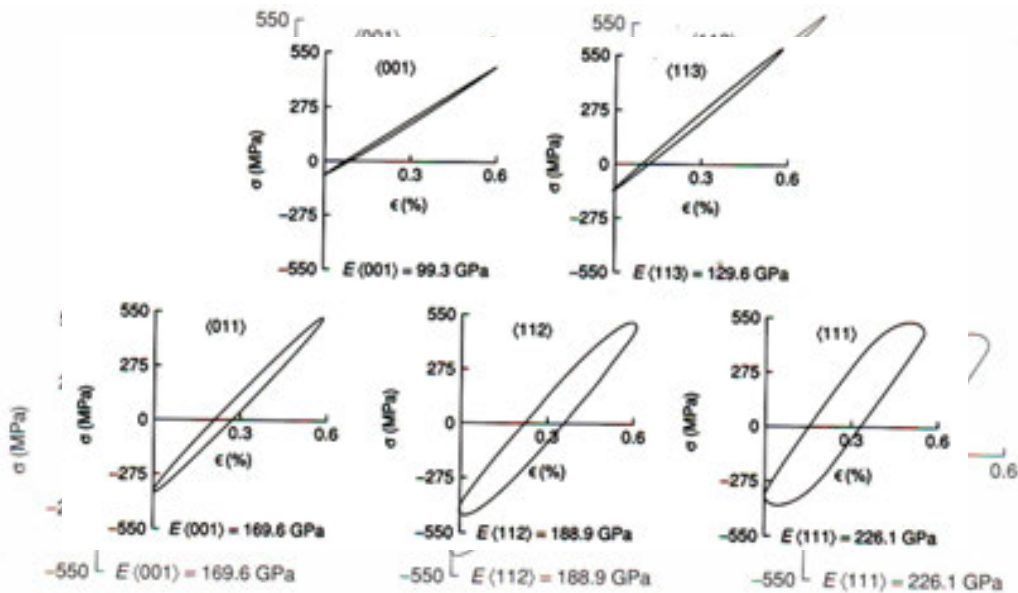

Figure 6. Effect of crystallographic orientation on fatigue hysteresis loops for an experimental SC superalloy at 980°C and with $\Delta\epsilon_{total} = 0.6$, $R = 0$. Data taken from reference [1].
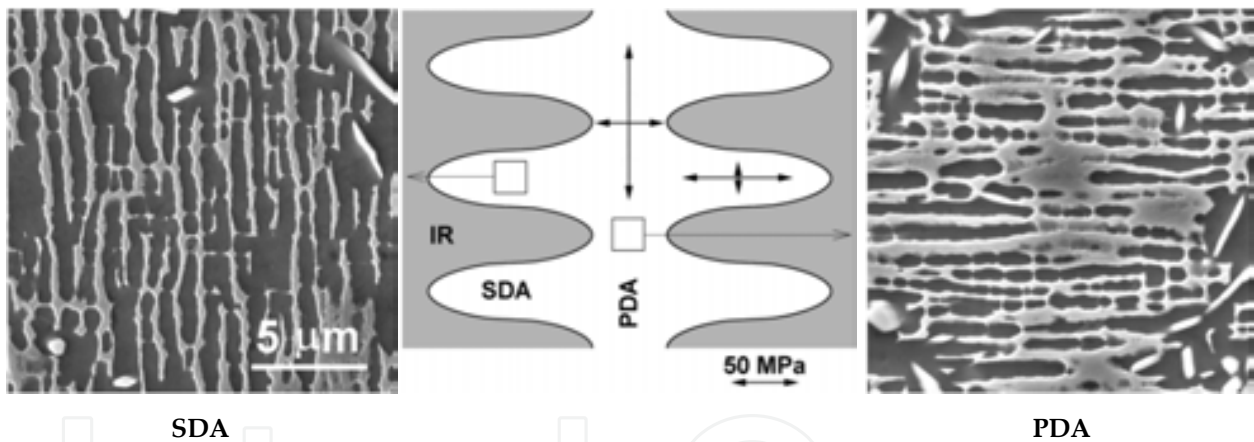
SDA   PDA

Figure 7. The γ/γ'-microstructure in the dendrite arms of CMSX-4 rafted during annealing at 1100°C under denritic stresses. Dendritic stresses estimated at 1100°C by FE modelling are shown by arrows. Adapted from reference [35].

The mechanical deformation of SC Ni-based superalloys has been theoretically studied by Huang et al. [36] and Yashiro et al. [37] via discrete dislocation dynamics (DDD) modeling. A transversely isotropic viscoelasticity model for a directionally solidified polycrystalline Ni-based superalloy has been developed by Shenoy et al. [38] to characterize the function of temperature and the stress-strain response has been studied at temperatures ranging from 427°C to 1050°C. These models indicate that mechanical deformation occurs because of interactions of super dislocations and the internal microstructure. The channel width and precipitate size both affect the flow stress and cyclic hardening or softening of SC Ni-based superalloys. The mechanical deformation in the viscoelastic-plastic field of SC Ni-based
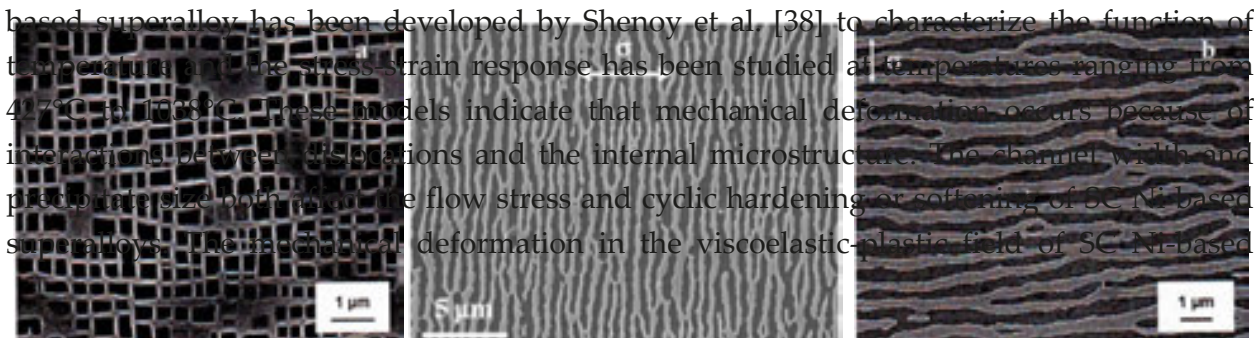
Figure 7. The γ/γ'-microstructure in the dendrite arms of CMSX-4 rafted during annealing at 1100°C under denritic stresses. Dendritic stresses estimated at 1100°C by FE-modelling are shown by arrows. Adapted from reference [35]
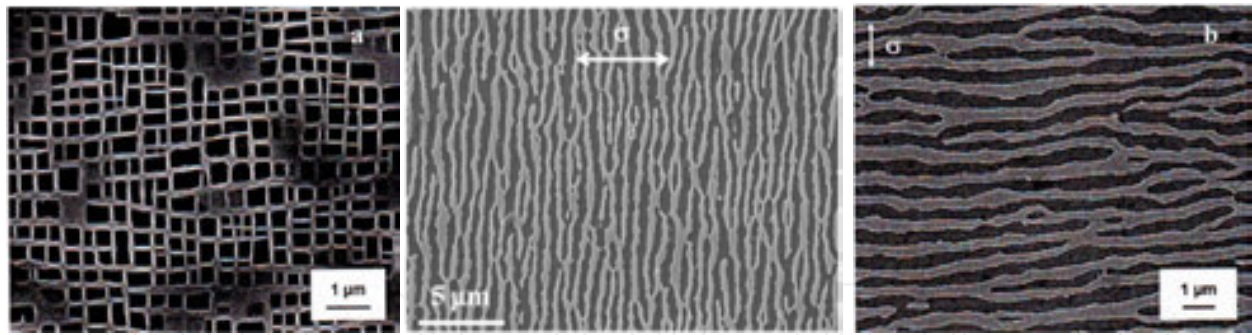

Figure 8. Microstructure of γ/γ'-phase in initial state (a) and at creep deformation formed different raft types. Adapted from reference [15].

superalloys under tension-compression cyclic loading [39] shows that the phases' chemical composition was changed. Instrumented indentation testing at elevated temperatures [40] and nanoindentation testing [41–43] of superalloys has been theoretically studied to understand the properties of these materials. This phonon micromechanical properties of SC Ni-based superalloys were studied, and the results show that Young's modulus evaluated by the Oliver–Pharr method, depends on the testing temperature [40], and it was lowered by increases in temperature. The micromechanical properties depend on chemical composition and collected strain [41–43]. It is well known that the turbine-entered temperature (TET) varies from ±60°C at ground idle for relatively short times. Some new methods have been developed for SC NI-based superalloys testing [44, 45] and the different gradually shaped specimens were used. Therefore, in this chapter, we studied the tension-compression stress amplitudes in the field of viscoelastic as well viscoplastic deformation during low number and low frequency of cycles at room temperature. By this method, the cyclic stresses influenced the interdiffusion of elements and atoms between different phases. This method of SC Ni-based superalloy testing is called hard cyclic viscoplastic (HCV) deformation [28, 39, 44, 46]. We estimated the micro-structure evolution, phase equilibria shifts, chemical composition phase changes, and changes in the micromechanical properties of different phases in SC Ni-based superalloys during HCV deformation at room temperature.

3. Materials and experimental procedures

3.1. Casting of SC Ni-based superalloy

The test material that was subjected to HCV deformation was the commercially available SC Ni-based superalloy ZS32-vi (Russian standard), which had the following composition (in at. %) of main elements: 12.1% Al, 5.3% Cr, 9.4% Co, 0.8% Nb, 0.9% Ta, 0.7% Mo, 2.5% W, and 0.7% Re, with the remainder being Ni. No Ti was present in this superalloy. The casts of the SC Ni-based superalloy samples were produced by NPO "A. Lylka-Saturn" via an electro-magnetic induction melting technique in a directional solidification furnace under high vacuum. The withdrawing rate was ~3.4 mm/min, which yielded solid casts with dendrites of up to ~4.5 mm in length. The as-received SC cast rods were 15 mm in diameter and ~160 mm

in length. We speculate that all of the cast test parts of samples possessed identical microstructures and properties before HCV deformation testing; as they were produced using identical technological parameters of casting [see 20-23].

3.2. Initial microstructure of SC cast Ni-based superalloy

The as-cast optical microstructure is shown in the longitudinal (001) direction in Figure 9 and in cross-section in Figure 10a, whereas the γ/γ' microstructure of a cast SC Ni-based superalloy ZS32-vi sample is presented in Figure 10b. The microstructure mine constituent's parts or details are shown in Figure 9 by arrows. As shown, the primary dendrites' length is about 4.5 mm and dendrite arm spacing is about 400-500 μm. The eutectic pools are situated near the primary dendrite axis and in the interdendritic region. Therefore, metal carbides with high concentrations of Nb/Ta content situated near eutectic pools (Figure 12 a) and metal carbides with lower Nb/Ta content in interdendritic region (Figure 12 b) between primary and secondary dendrite axis with γ/γ' microstructure. The phases under consideration in this study are presented in Figure 11. These phases are listed in Figure 11b: (a) primary dendrite axis (PDA) in (001) direction; (b) interdendritic region (IDR) with C-Nb/Ta-arrows (Figure 10); (c) secondary dendrite axis (SDA); (d) eutectic pools (EUT) with partly single γ'-phase in interdendritic region; and (e) Nb/Ta-rich metal carbides (MC) near EUT.
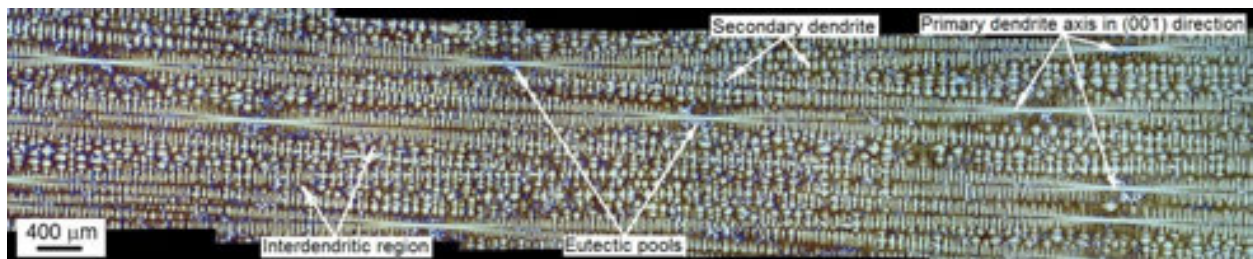

Figure 9. Microstructure of as-cast SC Ni-based superalloy ZS32-vi in longitudinal (001) direction. The microstructure elements are shown by arrows. Adapted from reference [46].
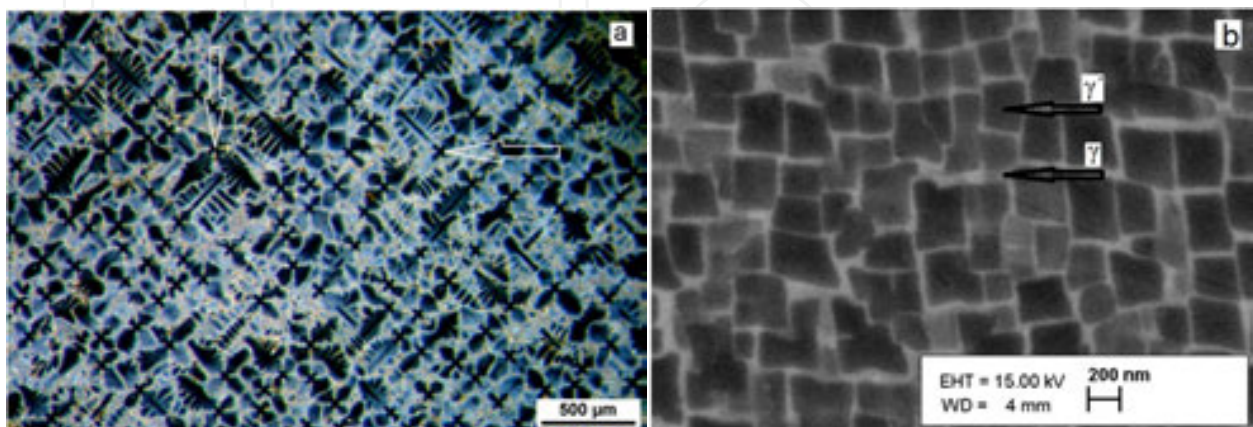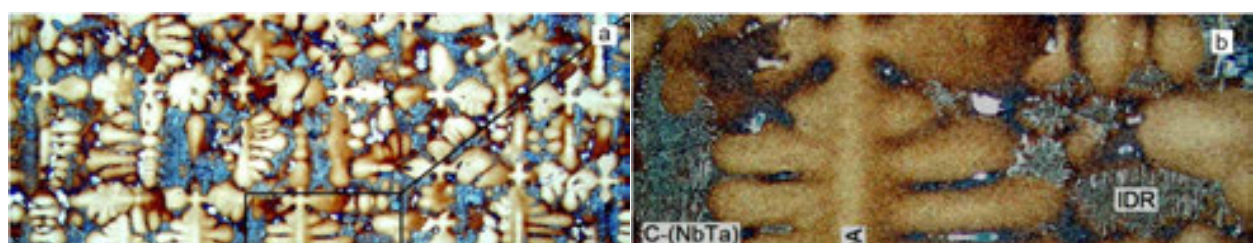

Figure 10. Microstructure of as-cast SC Ni-based superalloy ZS32-vi in cross-section of rod (a) and γ/γ'-phase (b). The primary dendrite quadrature axis and γ and γ' phases are shown by arrows.

Figure 9. Microstructure of as-cast SC Ni-based superalloy ZS32-vi in longitudinal (001) direction. The microstructure elements are shown by arrows. Adapted from reference

Figure 10. Microstructure of as-cast SC Ni-based superalloy ZS32-vi in cross-section of rod (a) and γ/γ´-phase (b). The primary dendrite quadrature axis and γ and γ´ phases are shown by arrows.

Figure 10. Microstructure of as-cast SC Ni-based superalloy ZS32-vi in cross-section of rod (a) and γ/γ´-phase (b). The primary dendrite quadrature axis and γ and γ´ phases are shown by arrows.

Figure 11. Microstructure of SC in the (001) direction (a) and magnification of dendrite microstructure (b) with the main tested phases which are under consideration. PDA, primary dendrite axis in (001) direction; IDR, interdendritic region with C-Nb/Ta-arrows; SDA, secondary dendrite axis; EUT, eutectic pools in interdendritic region; MC, Nb/Ta-rich metal carbides. Adapted from references [39, 46].
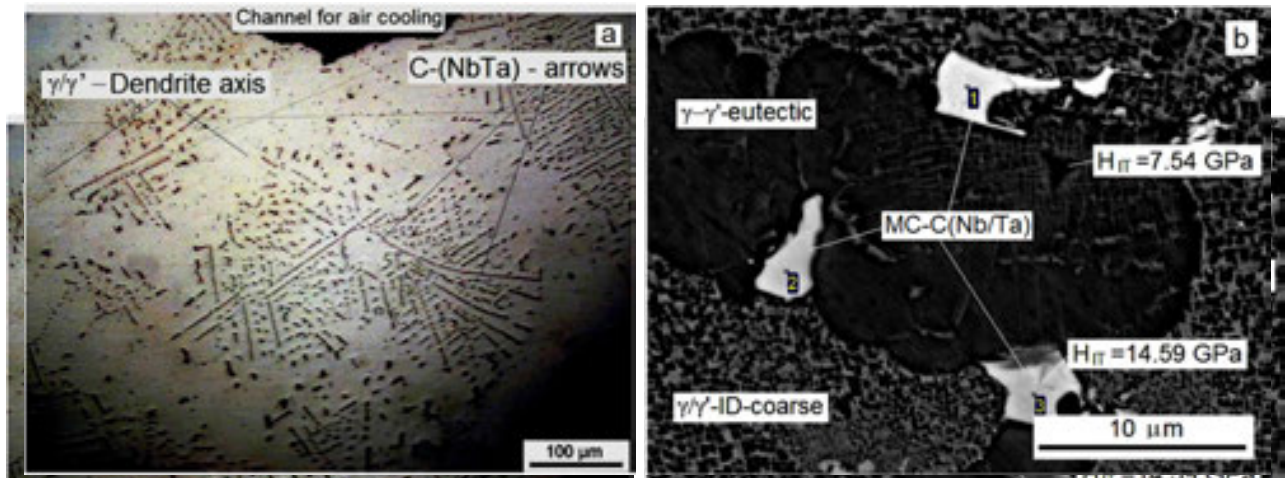

Figure 12. Interdendritic region in turbine blade cross-section with air cooling channel (top) and C-(Nb/Ta)-metal carbide complex (arrows) for reinforcement of the interdendritic region (a) and MC near the eutectic pool in the interdendritic region (b).

4. Proposed test methods and results

4.1. Hard cyclic viscoplastic deformation

HCV deformation was done using an Instron 8516 materials testing installation at room temperature in the Materials Testing Laboratory at the Department of Material Engineering of Tallinn University of Technology, Estonia. In the present chapter, we studied the behavior of single crystalline Ni-based superalloy ZS32-vi for turbine blade application in aircraft

turbojet engine AL-31-F. The SC material was tested at room temperature. We estimated the shift in the phase equilibria of an SC Ni-based superalloy during HCV deformation. The method we used was based on the Bauschinger effect. The objective of the present work was to study the role played by the deformation-assisted interdiffusion of atoms among different phases in shifting the phase equilibrium, which was characterized based on the evolving chemical composition and micromechanical properties of each investigated phases (see Figure 11 b). In my opinion, such an investigation can provide realistic information concerning the shifts in the phase equilibria of SC Ni-based superalloys under HCV deformation in start-up regime at ground idle temperature (±60°C) of turbine blades of turbojet engines. The specimens for HCV deformation were cut with stepped cross-sectional areas from the SC casts with dimensions of 16 mm in diameter and ~160 mm in length. The cross-sectional areas of the tension-compression specimens for HCV deformation (Figure 13) were 200 mm^2, 154 mm^2, 77 mm^2, and 38.5 mm^2 for test samples S1, S2, S3, and S4, respectively. The test parts were 12 mm long with a radius of 3 mm. The extensometer that was used to measure the true strain had a base length of 10 mm and was mounted on the test part (S4) with the smallest cross-section (38.5 mm^2). The stress values for the other cross-sections were calculated and found to decrease proportionally with the increase in the cross-section (Figure 14).
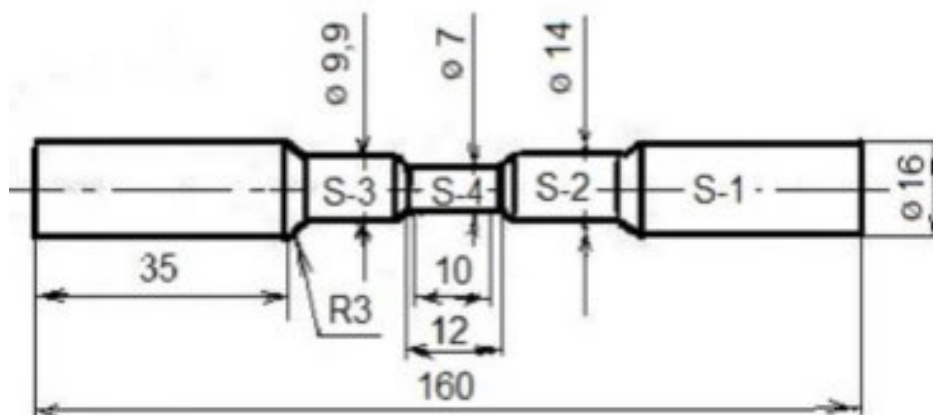

Figure 13. Scheme of the sample for HCV deformation. Designations in mm. Adapted from references [44, 46].

The cross-sections for samples S4, S3, and S2 increased twice as much per step relative to the next section. The HCV deformation tests were conducted using tension/compression-strain amplitudes of 0%–0.05%, 0%–0.2%, 0%–0.5%, and 0%–1% for 30 cycles at each strain amplitude. After such straining, the samples were fractured at tension strain of 1.5%. The cycling frequency was 0.5 Hz and remained constant for all strain amplitudes. The strain rates increased with increasing strain amplitudes. These strain amplitude values were experimentally chosen. The specimen length for HCV deformation was identical before and after cycling. Because the test sample (see Figure 13) has gradually shaped cross-sections, the stress and strain amplitudes decrease proportionally to increases in the cross-sectional areas. The collected maximal stress amplitude curves in sample S4 of testing for all strain amplitudes in Figure 15 are presented. As shown in the graphs at strain amplitudes of 0%-0.05%, 0%-0.2%, and 0%-5%, the
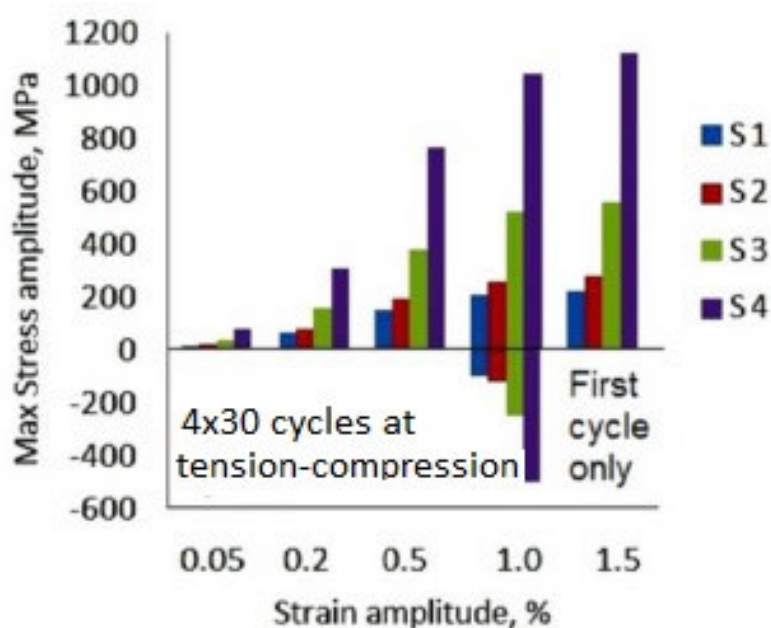
Figure 14. Maximal stress amplitude values (calculated) at tension and at compression for corresponding strain amplitudes in samples S1, S2, S3, and S4, respectively. Adapted from reference [3]

maximal stress values decrease slightly but the material shows fully viscoelastic behavior. The hysteresis loops were not formed as previously seen during conventional test method, which is presented in Figure 6. By increasing the strain amplitude, the stress amplitude increased proportionally. By increasing the strain amplitude to 0%-0.5%, the stress at tension increased up to 770 MPa at the first cycle and then decreased to 745 MPa at the end of cycling. The stress amplitudes decreased slightly under constant strain. This result indicates that the material does not harden due to an increase in the dislocation density. This standpoint (dislocation density increase) was presented by a large number of works listed in the references [36-38]. A discrete dislocation dynamic model [36, 37] was used to characterize the mechanical defor- mation and softening of the Ni-based superalloys SC. This model shows that the precipitates sheared by super dislocations were responsible for softening the SC Ni-based superalloy. Such softening behavior is presented in Figure 15b, d, and f. At maximal strain amplitude of 0%-1%, the tension stress at first cycle was maximal and then decreased during 2-3 cycles. Afterward, the stress amplitude maximal values do not decrease during the following cycles. The time- stress curves at strain amplitude of 0%-1% for the first, second, and 30 cycles are shown in Figure 16, and the summarized strain-stress curves are shown in Figure 17.

Experimental works [39, 44] demonstrate an identical behavior for SC Ni-based superalloys ZS32-vi during HCV deformation. During the first cycle of the present study (Figures 17 and 18), sample S4 was plastically elongated during the tension cycle starting at a strain of 0.65% to a strain of 1.03%. After this plastic elongation, sample S4 was compressed to zero (to the initial length) using a ~500 MPa stress. The curves for 0-I, 0-II, and 0-III overlap, and the material demonstrates a fully viscoelastic behavior. The plastic elongation (PL) of the material during viscoelastic cycling occurs from strains from 0.65% to 1.03%. For the first three test series (0-I,
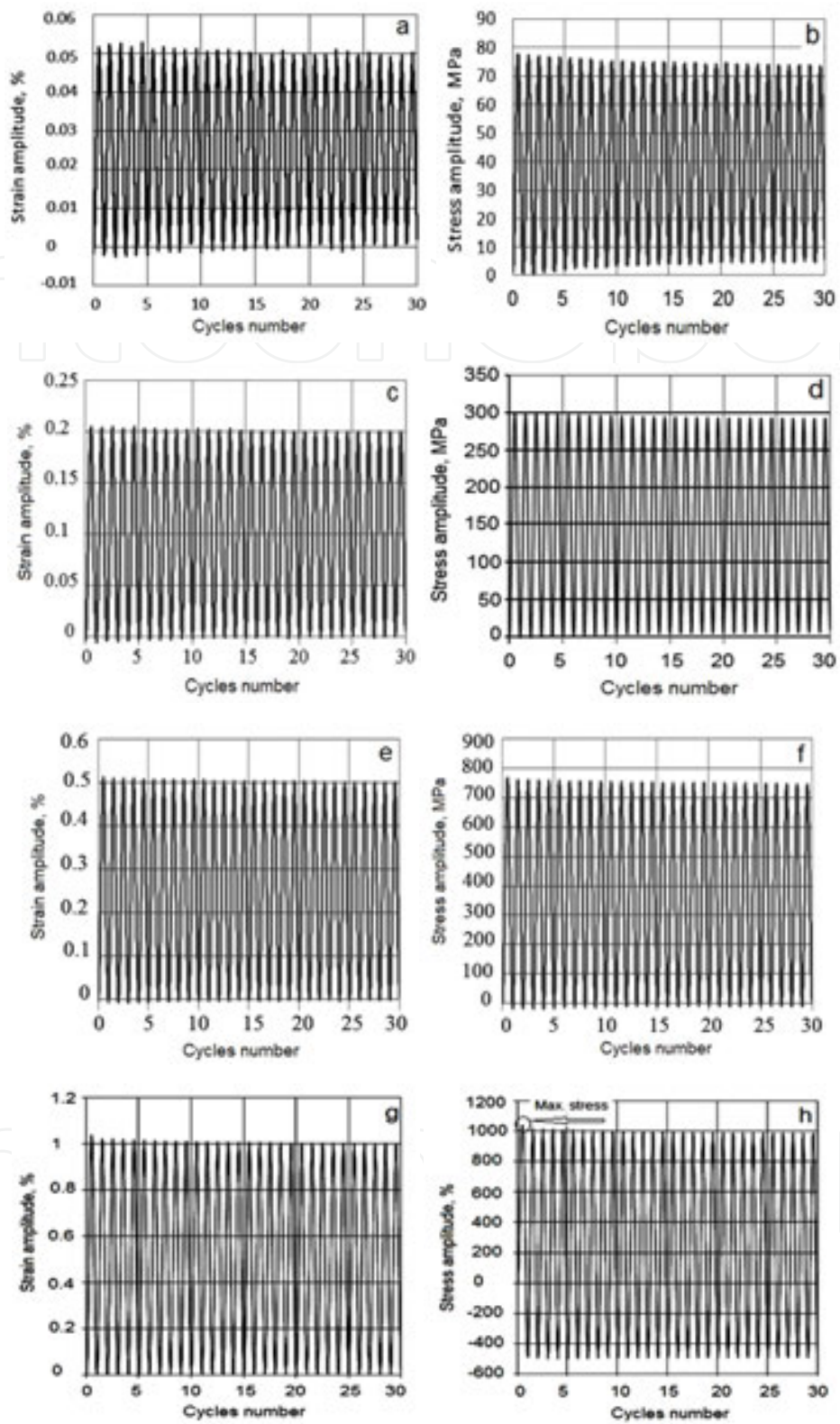
Figure 15. The strain amplitudes at 0.05%, 0.2%, 0.5%, and 1% (a, c, e, and g, respectively), and corresponding to the stress amplitudes (b, d, f, and h, respectively) in the SC of Ni-based superalloy ZS32-vi.
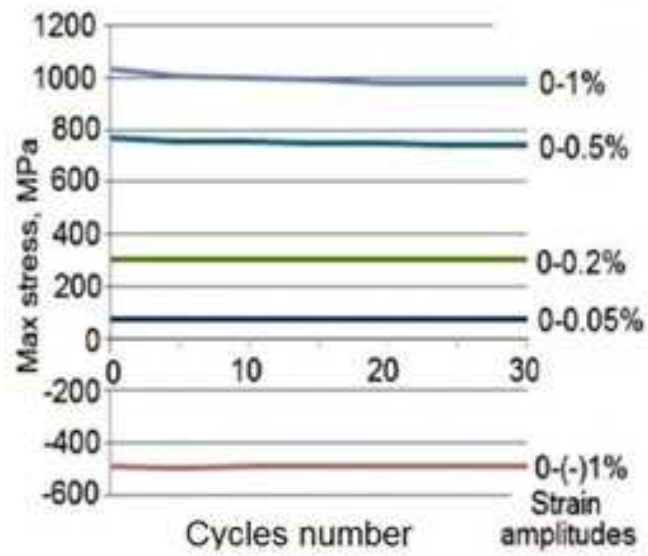
Figure 16. Maximal stress values evolution of 30 cycles measured in sample S4 for tension-compression strain amplitudes of 0%-0.05%, 0%-0.2%, 0%-0.5%, and 0%-1%, respectively. Adapted from reference [46].
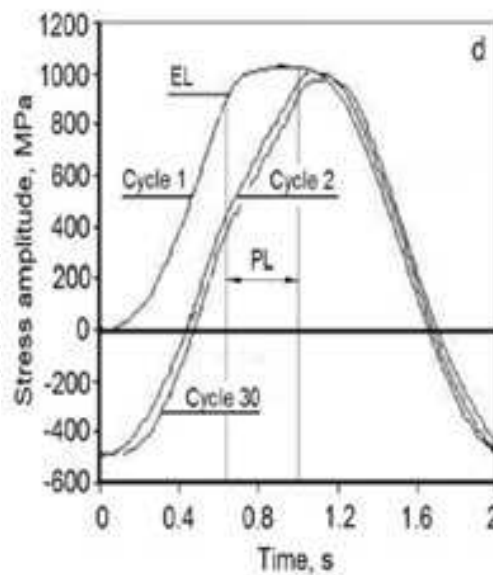

Figure 17. Time-dependent stress amplitudes shift at first, second, and 30 cycles for strain amplitude of 0%-1%, respectively.
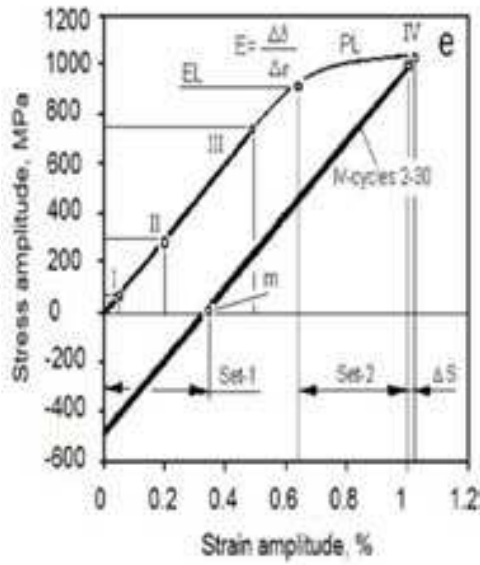
Figure 18. The graph summarizes the strain-stress curves of the SC Ni-based superalloy for the 38.5 mm² cross-section during the HCVD testing. The definitions are as follows: 0-I, stress-strain curve at a strain amplitude of 0%-0.05% for 30 cycles; 0-II, at 0%-0.2%; 0-III, at 0%-0.5%; 0-IV, the portion of the tension curve during the first tension cycle at a strain of 1%; and IV, cycles 2-30–stress-strain curves at a strain amplitude of 0%-1%; ΔS, ~0.03% strain is the system error; Set-1 ≅ Set-2, part of the plastic deformation during the first compression cycle in the fourth series; PL, proportional limit; EL, elastic limit; and "m", starting point of the material compression. Adapted from references [28, 39, 44].
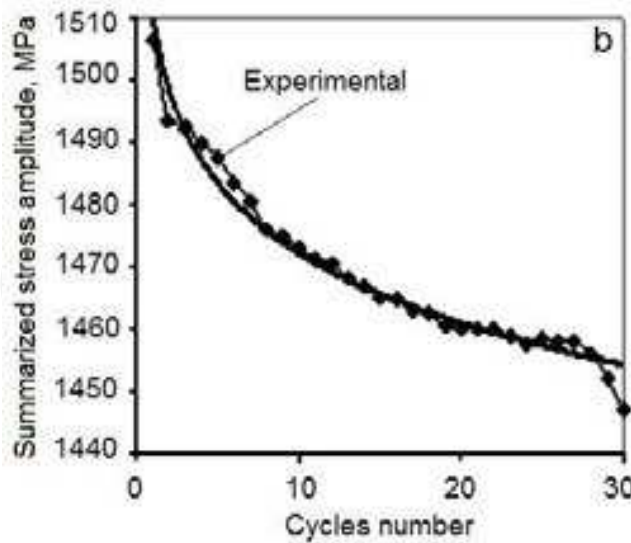

Figure 19. The absolute (summarized) reduction of the tension-compression stress amplitude for strain amplitudes from 0% to 1% for sample S4 during HCV deformation. Adapted from reference [44]

0-II, and 0-III), all of the stress-strain curves overlap and exhibit a linear dependence; therefore, the material is showing a fully elastic behavior and Young's modulus does not change. Increasing the tension strain of the first cycle from the start of the plastic deformation, 0.65%, elongates the sample (in the center, which is a cross-section of 38.5 mm) up to a strain of 1.03%. The extra 0.03% (over 1%) is shown in the graph as ΔS in Figure 18. The curve decreased from point "m" to the stress axis once the sample was compressed using ~500 MPa during the first cycle. The absolute (summarized) tension-compression amplitude reduction is shown in Figure 19. At the first two cycles and at the end of three cycles, the summarized stress amplitude decreases sharply, which indicates the softening behavior of SC materials at these cycles.

4.2. Nanoindentation: Micromechanical properties of phases

The micromechanical properties of the phases were characterized using a nanoindentation device from the NanoTest NTX testing center (Micro Materials Ltd.). This installation is presented in Figure 20. A diamond Berkovich tip with a three-sided pyramid apex angle of 142.3° and a radius of 100 nm was used for these measurements. This installation was equipped with an optical microscope to search for nanometer measurements of indented points on the diamond-ground surfaces of the samples. The nanoindentation tests were conducted on diametric sections of the samples. The following phases were investigated via scanning electron microscopy in combination with the energy-dispersive spectrometry system and nanoindentation: fine γ/γ', coarse γ/γ', eutectic γ-γ', and metal carbide (MC) phases. The MC phases contained Nb/Ta intermetallic compounds. The nanoindentation tests were conducted on diametric sections of the samples. The samples were mechanically ground and etched to indicate the dendrite direction.
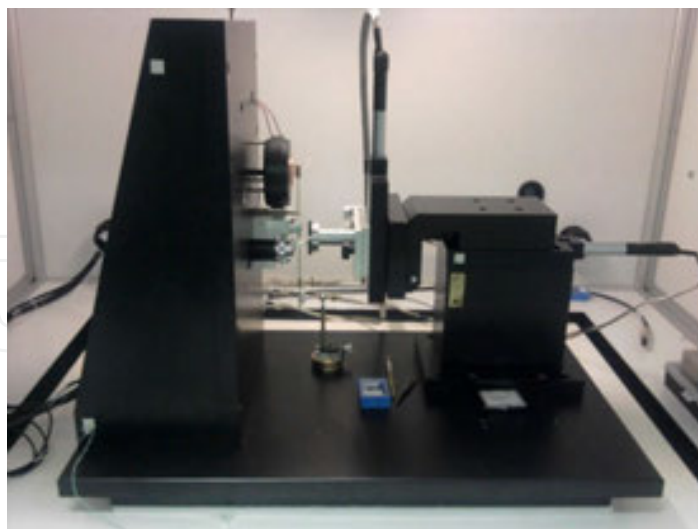

Figure 20. Nanoindentation setup NanoTest NTX testing center (Micro Materials Ltd.) used for phase micromechanical property measurements in this investigation.

An optical image of the as-cast microstructure is presented in Figure 9. The microstructures with corresponding indent points of phases in the testing regions of the samples are presented

in Figure 21a, b, c, and d. In one study [3], 100 indents were made in all samples in a row with a 20-µm step over a distance of 2 mm using a load of 15 mN. The rows of nanoindentation are perpendicular to the (001) direction of the cast. The micromechanical properties of the phases were studied for all 400 test points (100 points per sample) from the SEM pictures of microstructures across all four samples. The maximal- and plastic depths of the indents were measured with high-precision installation (see Figure 20). The micromechanical properties were calculated automatically by computer according to the Oliver-Pharr method and presented in tables. According to table dates, the corresponding graphs of micromechanical properties of phases were built and are presented in Figures 22, 23, and 24, respectively. Changes in the microstructure occur under the viscoplastic strain conditions (shown in Figure 28). The micromechanical properties and their ratios from both before and after the HCV deformation study are shown [3] to demonstrate how the micromechanical properties of the phases were changed by the interdiffusion of various atoms (studied below). The nanoindentation test results show (Figure 22a) that the maximal and plastic indentation depths of the phases decreased with increases of the collected strain in samples, which depends on stress amplitude increases (see Figure 14). The mean of the micromechanical properties for all of the phases across all samples were calculated and are presented in Figures 22, 23, and 24. The micromechanical properties of the investigated phases were calculated according to the received/measured maximal and plastic indentation depths under a 15 mN load. Our previous work [3] showed that, for nanoindentation, the results depend on the load used. Therefore, the results of nano- and microindentation measurements (see in [3], Figure 9a and b) show approximately identical distributions of hardness values for all analyzed phases. The dependence of the nanoindentation test results on the applied load was previously studied by Neumeier et al. [43], Schöberl et al. [47] and Kommel et al. [3]. The mean (M) nanohardness (Figure 22b) shows that it increased stepwise with increasing cumulative strain (decrease of indentation depth; Figure 22a). The nanohardness and elastic modulus also increased for all of the samples and phases (Figures 23b and 24a). Additionally, the plastic and elastic work of the indentation (Figure 23b), elastic recovery parameter (Figure 24a), and contact compliance parameter (Figure 24b) all decreased.

The micromechanical properties and elemental ratios of the samples and phases were initially studied in [3]. The microhardness of the coarse γ/γ'-phase increased sharply relative to the fine γ/γ'-phase microhardness. The microhardness ratio decreased from 1.3 to 1.09 as the hardness of the coarse γ/γ'-microstructure increased. This increased hardness was predicted by the increase in the $\gamma-\gamma'$-eutectic pools surfaces at higher strain (shown below). For example, increasing the nanohardness decreased the contact compliance parameters but significantly increased the plastic and elastic portions of the indentation work. The elastic recovery parameter (Figure 24a) decreased during the HCV deformation similar to the elevated temperatures measured during microindentation in [39]. The results from this nanoindentation (Figure 23a) indicate that the modulus of elasticity (E_r) increased because the cumulative sample strain increased. The mean E_r increased from 200 GPa in as-cast SC to ~340 GPa and mean nanohardness from 12.8 GPa to 16 GPa after HCV deformation. The micromechanical properties and their ratios before and after the HCV deformation study are presented to
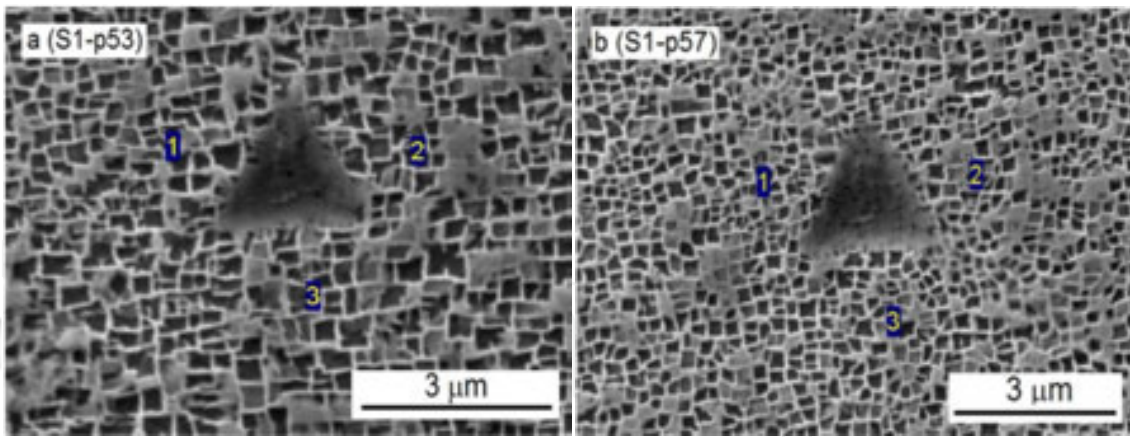
Figure 21. Nanoindentation triangular test points in the γ/γ'- coarse (a), γ/γ'- fine (b), γ-γ'- eutectic pool (c), and C(Nb/Ta)-MC (d) phases. The chemical elemental compositions of the three measured points by SEM-EDS in these phases are shown near the indents. Adapted from reference [46].
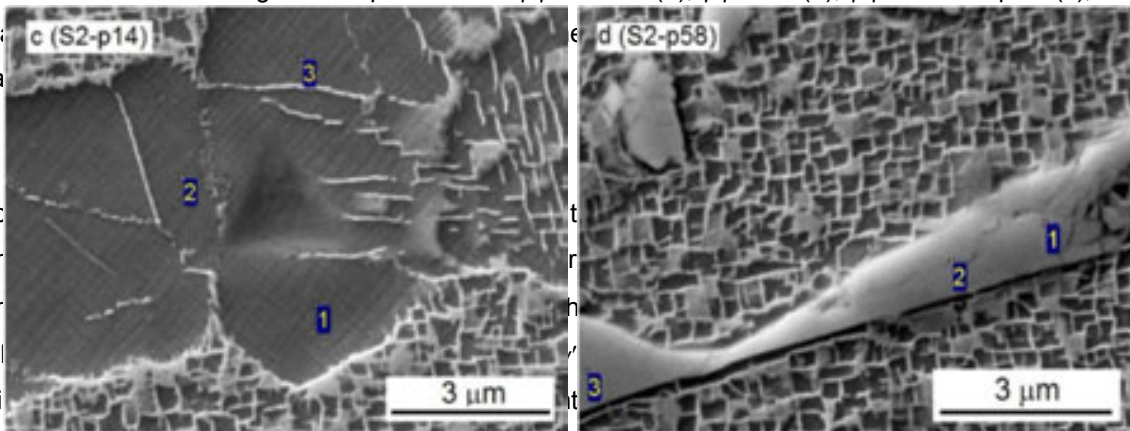
The micromechanical properties and elemental ratios of the samples and phases were initially studied in [3]. The microhardness of the coarse γ/γ'-phase increased sharply relative to the fine γ/γ'-phase microhardness. The microhardness ratio decreased from 1.3 to 1.09 as the hardness of the coarse γ/γ'-microstructure increased. This increased hardness was predicted by the increase in the γ-γ'-eutectic pools surfaces at higher strain (shown below). For example, increasing the nanohardness decreased the contact compliance parameters but significantly increased the plastic and elastic portions of the indentation work. The elastic recovery parameter (Figure 24a) decreased during the HCV deformation similar to the elevated temperatures measured during microindentation in [39]. The results from this nanoindentation (Figure 23a) indicate that the modulus of elasticity (E_r) increased because the cumulative sample strain increased. The mean E_r increased from 200 GPa in as-cast SC to ~340 GPa and mean nanohardness from 12.8 GPa to 16 GPa after HCV deformation. The micromechanical properties and their ratios before and after the HCV deformation study are presented to demonstrate the change in the micromechanical properties of the phases caused by the interdiffusion of various atoms.

Figure 22. In addition to the maximal and plastic indentation depths, the MM_r (mean value for 100 indents) of the test points was measured under a 15 mN load (a) and calculated nanohardness (b). Designations: M, mean values across 100 tests (according to the tabulated data); C, coarse γ/γ'-phase; F, fine γ/γ'-phase; E, γ-γ' eutectic phase; and MC, Nb/Ta-MC phase.
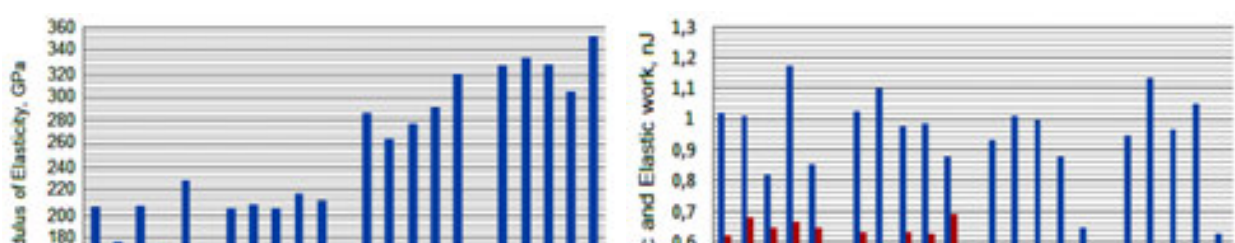
Figure 22. In addition to the maximal and plastic indentation depths, the "M", (mean value for 100 indents) of the test points was measured under a 15 mN load (a) and calculated nanohardness (b). Designations: M, mean values across 100 tests (according to the tabulated data); C, coarse γ/γ'-phase; F, fine γ/γ'-phase; E, γ-γ' eutectic phase; and MC, Nb/Ta-MC phase.
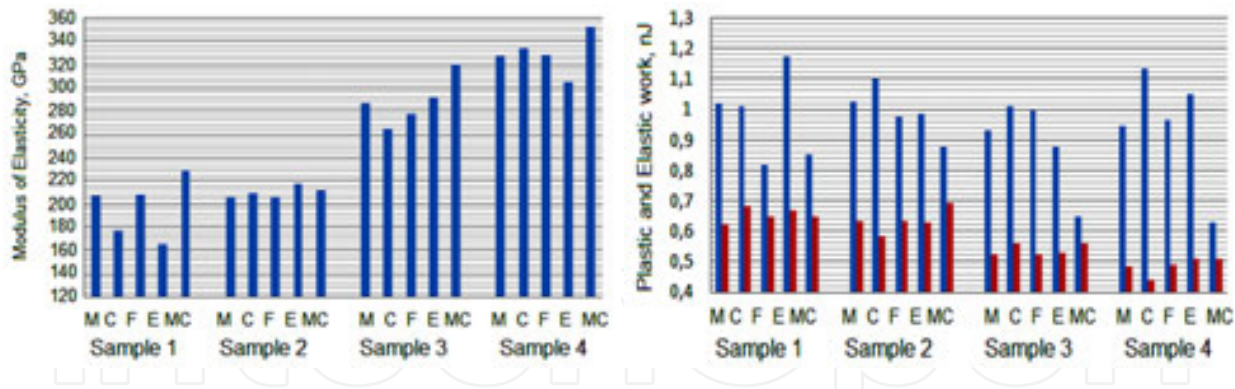

Figure 23. The phase dependence of the elastic modulus (a) and both the plastic and elastic work (b) for samples from collected strains. Designations such as those in Figure 22 are shown.
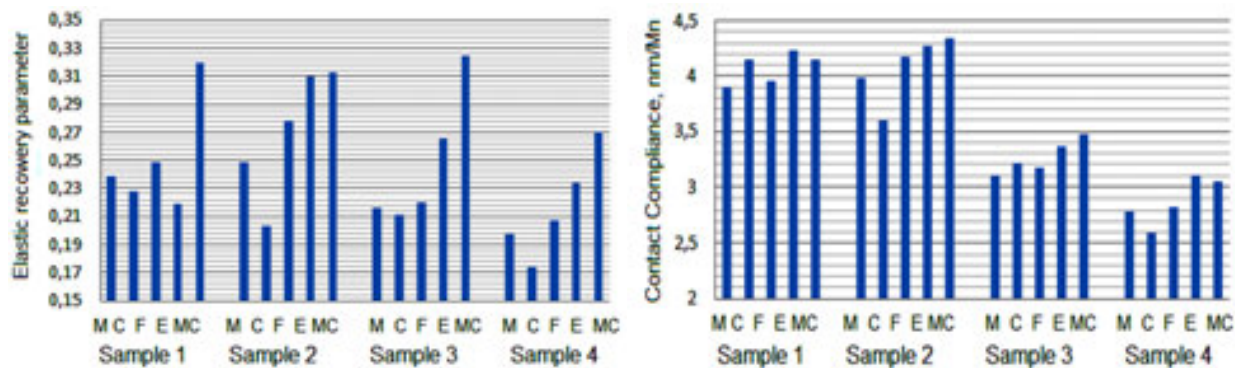

Figure 24. The phase dependence of the elastic recovery (a) and contact compliance (b) parameters for samples under cumulative strain. Designations such as those in Figure 22 are shown.

This work strongly indicates that such changes in the micromechanical properties of the phases is dependent on the change in the chemical concentration of the phase after interdiffusion. The micromechanical properties and elemental ratios of the samples and phases initially evolved are studied. The effect atomic interdiffusion had on the evolution of the micromechanical phase properties has been defined as a ratio of these properties [25, 28]. The microhardness of the coarse γ/γ'-phase increased sharply relative to the fine γ/γ'-phase microhardness. The microhardness ratio decreased from 1.3 to 1.09 as the hardness of the coarse γ/γ'-microstructure increased. This increased material hardness was predicted by increases in the γ-γ'-eutectic phase pool's surfaces (Figure 26) at higher strain.

4.3. Microstructural analysis of phases

Depending on the processing parameters (temperature gradient, withdrawal velocity, etc.) by directional solidification [20-23], the solidification parameters influence the length of the dendrites and the spacing of the microstructure. The experimental results of measured dendrite arm spacing [1, 47] are presented in a graph (Figure 25). The dendrite spacing of some commercial superalloys lies from 50 to 600 μm (Figure 25). In this study, SC superalloy ZS32-vi with a dendrite spacing of 350-400 μm and dendrite length of up to 4 mm, respectively, was used (see Figures 10-13). The width of a γ-phase channels was about 100-200 nm in the PDA region and about 300-400 nm in the ID region (see Figure 21a and b), respectively. During HCV deformation (at room temperature) the atoms interdiffusion between different phases was induced and the dendrite measures decreased (Figure 26 and 27).

vi with a dendrite spacing of 350-400 μm and dendrite length of up to 4 mm, respectively, was used (see Figures 10-13). The width of a γ-phase channels was about 100-200 nm in the PDA region and about 300-400 nm in the ID region (see Figure 21a and b), respectively. During HCV deformation (at room temperature) the atoms interdiffusion between different phases was induced and the dendrite measures decreased (Figure 26 and 27).
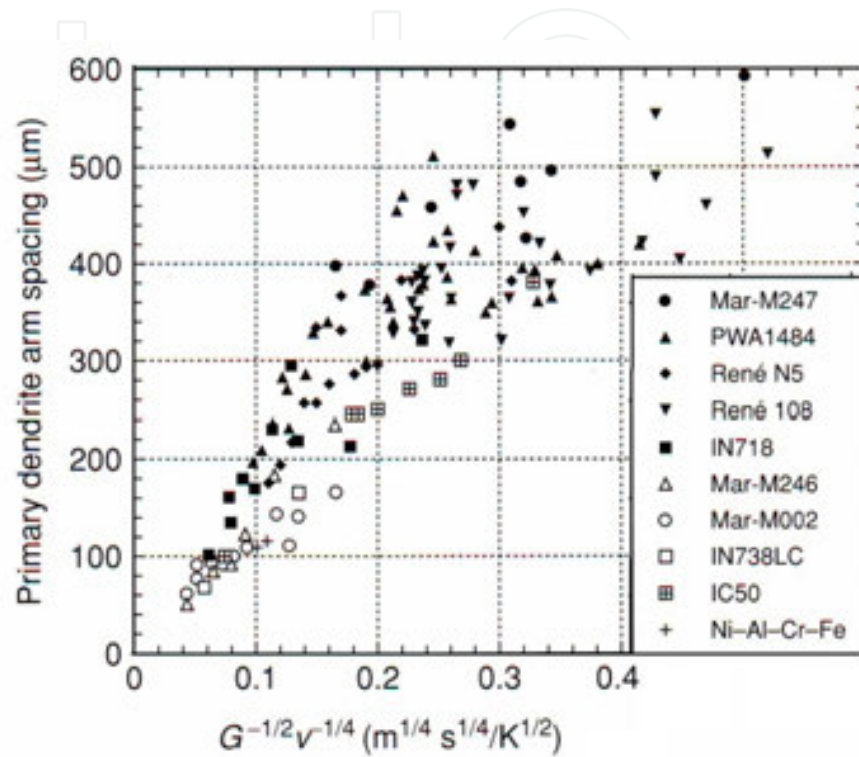

Figure 25. Some commercial superalloys' primary dendrite arm spacing with the combination $G^{-1/2}v^{-1/4}$, where G is the temperature gradient and v is the withdrawal velocity. Adapted from references [1, 47].
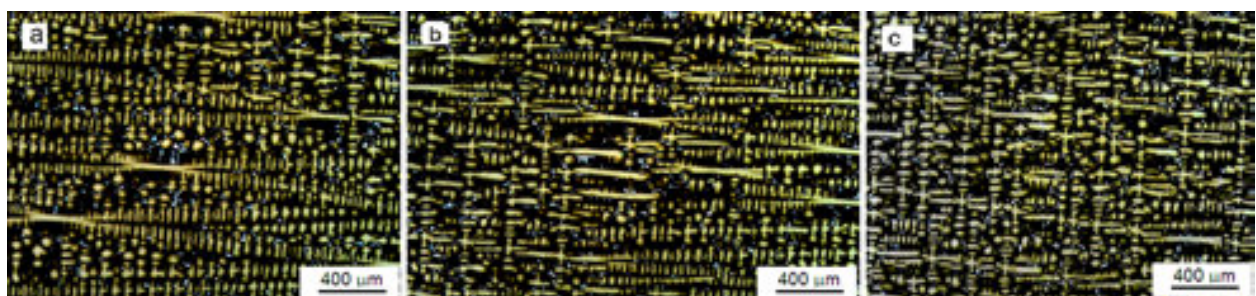

Figure 26. Optical micrographs of the SC Ni-base superalloy ZS32-vi dendrites measure stepwise decreases in samples S2, S3, and S4 during HCV deformation. The corresponding stress-strain amplitudes are presented in Figure 14. Adapted from reference [46]

The number and area of the γ-γ′-phase eutectic pools relative to the microstructure increased stepwise: S1, 1.05%; S2, 1.14%; S3, 1.86%; and S4, 2.06%. This development of the γ-γ′-phase eutectic pools is presented in Figure 27. The formation and distribution of these pools were

Figure 26. Optical micrographs of the SC Ni-base superalloy ZS32-vi dendrites measure stepwise decreases in samples S2, S3, and S4 during HCV deformation. The corresponding stress-strain amplitudes are presented in Figure 14. Adapted from reference [46]
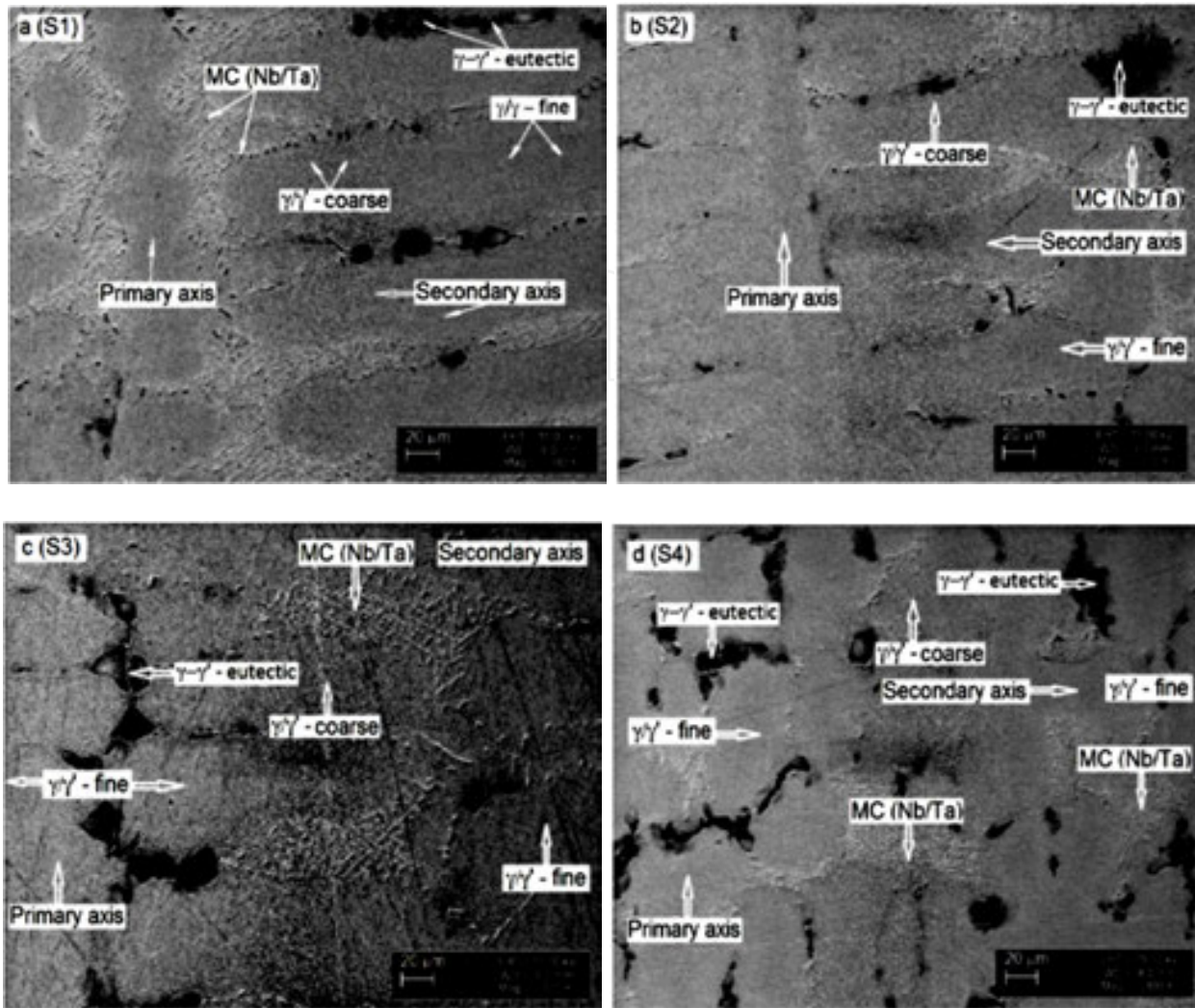
Figure 27. Eutectic pools evolution on primary dendrite area with γ/γ'- fine microstructure of samples S1, S2, S3, and S4, respectively, as a result of atom interdiffusion during HCV deformation. Adapted from reference [46 (a and d)].

investigated on the 3 mm² surfaces of all samples. Starting from sample S2, the new γ-γ'-phase eutectic pools took form with increasing strain amplitudes. As shown in the figure, the primary axes of samples S3 and S4 were crossed with new γ-γ'-phase eutectic pools (Figure 27c and d), which formed the finer microstructure of the primary dendrites (Figure 26c). Such micro-segregation-induced inhomogeneity in the γ-γ'-phase eutectic pools has been found to occur in Ni-based SC superalloys at high temperatures [26]. There are two approaches to studying the diffusion and melting processes in SC superalloys: the absolute reaction-rate theory and the dynamic theory of diffusion [27]. These theories indicate that the diffusive motion of atoms primarily depends on the amplitudes of oriented vibrations and the surroundings. The diffusion activation energy varies with the size, atomic weight, and charge of the diffusing species. Hence, it is different for different elements (see Figures 2-5). In this study, this activation energy was provided by HCV deformation at room temperature and was expected to vary with the strain amplitude.

4.4. Elemental concentration analysis

The changes in the elemental concentrations of the coarse γ/γ'- phase (a), γ/γ'-fine phase (b), γ-γ'-eutectic phase (c), and Nb/Ta-rich MC phase (d) are plotted in Figure 28. The Al concentration was higher in the coarse γ/γ'-phase (Figure 28a) than in the fine γ/γ'-phase (Figure 28b). The increase in the Al content of the coarse γ/γ'-phase can be attributed to Al that originated from the γ-γ'-eutectic phase (Figure 28c) and the MC phase (Figure 28d), and was transported into the coarse γ/γ'-phase through the increase in the cumulative strain. Cr, Co, and Mo possess lower activation energies than Al, and their concentrations increased primarily in the γ/γ'-eutectic phase (Figure 28c), also originating from the coarse γ/γ'-phase and the MC phase (Figure 28d).
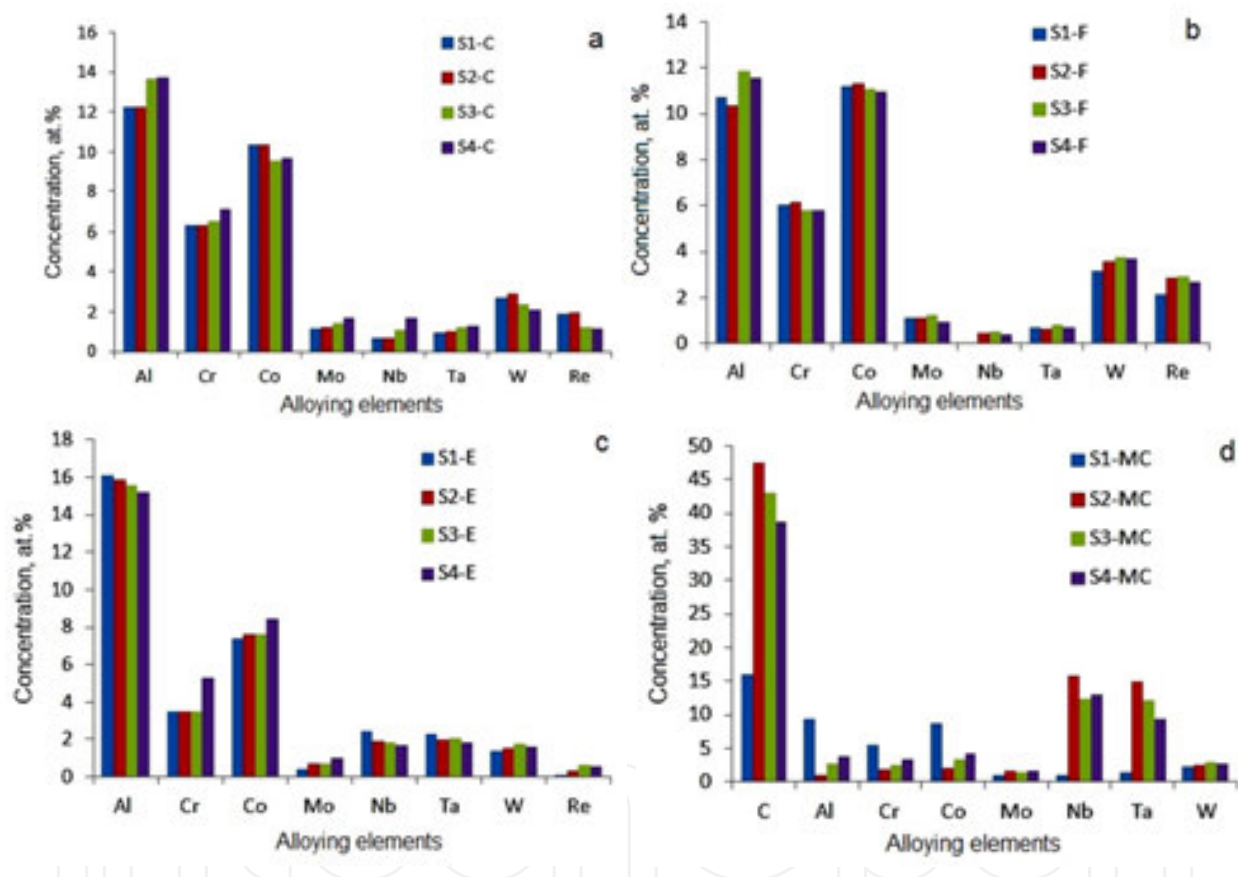

Figure 28. Elements concentration changes in coarse γ/γ'-phase (a), in fine γ/γ'-phase (b), in γ-γ'-eutectics phase pools (c), and in MC phases (d) of samples S1, S2, S3, and S4, respectively.

It is well known that an increase in Re and W content can increase the hardness and elasticity modulus of the γ-phase matrix [48]. The changes in the Nb/Ta concentration in the MC phase during the HCV deformation are illustrated in Figure 28d. The Nb/Ta-rich MC phases also contained a large amount of C and very small amounts of Ni, Cr, and Co. The MC phase did not contain Re. A detailed investigation of the MC phase revealed that the C, Nb, and Ta concentrations of the MC phase in the ID region cumulative strain eutectic phase pool MC (see Figure 12b). Based on this investigation, the diffusion directions of various elements are shown in the sample cross-sections by the arrows in Figure 29. A large number of energy-dispersive spectrometry investigations demonstrated that Al diffused along the dendrite axis, whereas Re and W diffused from the coarse γ/γ'-phase into the fine γ/γ'-phase and partly into the γ-γ'-eutectic phase pools. Therefore, the Al diffused into the dendrite axis from the γ-γ'-phase eutectic pools. Cr, Mo, and Co diffused into the γ-γ'-phase eutectic pools, whereas the MC, Ta, and Nb diffused into the fine γ/γ'-phase. The elemental concentrations of phases changed as a result of interdiffusion. Orlov

Figure 29. Mine directions of atom diffusion between phases in a cross-section of the primary axis is shown. Adapted from reference [46]

this investigation, the diffusion directions of various elements are shown in the sample cross-sections by the arrows in Figure 29. A large number of energy-dispersive spectrometry investigations demonstrated that Al diffused along the dendrite axis, whereas Re and W diffused from the coarse γ/γ'-phase into the fine γ/γ'-phase and partly into the γ-γ'-eutectic phase pools. Therefore, the Al diffused into the dendrite axis from the γ-γ'-phase eutectic pools. Cr, Mo, and Co diffused into the γ-γ'-phase eutectic pools, whereas the MC, Ta, and Nb diffused into the fine γ/γ'-phase. The elemental concentrations of phases changed as a result of interdiffusion. Orlov [49] previously detected such atomic interdiffusion among diff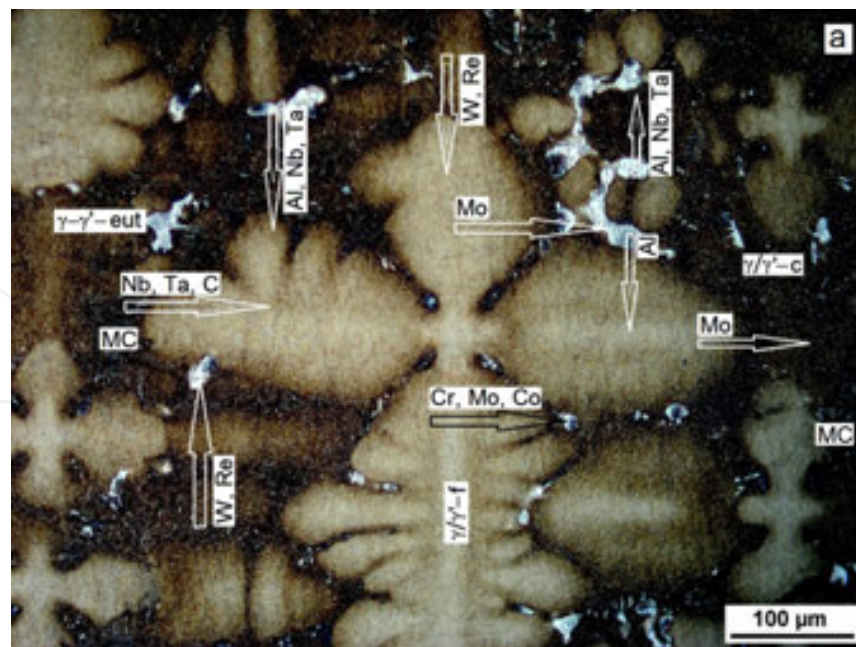erent phases and also found that diffusion pores form during the high-temperature heat treatment of superalloys (Figure 29). Such elemental motion at high temperatures changes the chemical compositions and micromechanical properties of the phases. In the present study, because of increased cumulative strain increase (or increased interdiffusion), small pores were formed in the coarse γ/γ'-phase or the interdendritic region of the superalloy. Such pores formed as a result of the high, unbalanced diffusion rate of Al in the Ni-based solid solution. It is well known from previous work [49] that diffusion pores form in metals during heat treatment or during long-term exposure at high temperatures because of the Kirkendall effect. Thus, the interdiffusion of elements during heat treatment as well as during HCV deformation at room temperature has identical mechanisms. As a result of the absence of balanced interdiffusion during HCV deformation, diffusion micropores (Figure 30a) and phase/grain boundaries could be formed (Figure 30b).

Such elemental motions change the chemical composition and micromechanical properties of the phases. At an increased cumulative strain and with the absence of balanced interdiffusion, the formation of small pores and phase boundaries (Figure 30) in the interdendritic region of

Figure 29. Mine directions of atom diffusion between phases in a cross-section of the primary axis is shown. Adapted from reference [46]
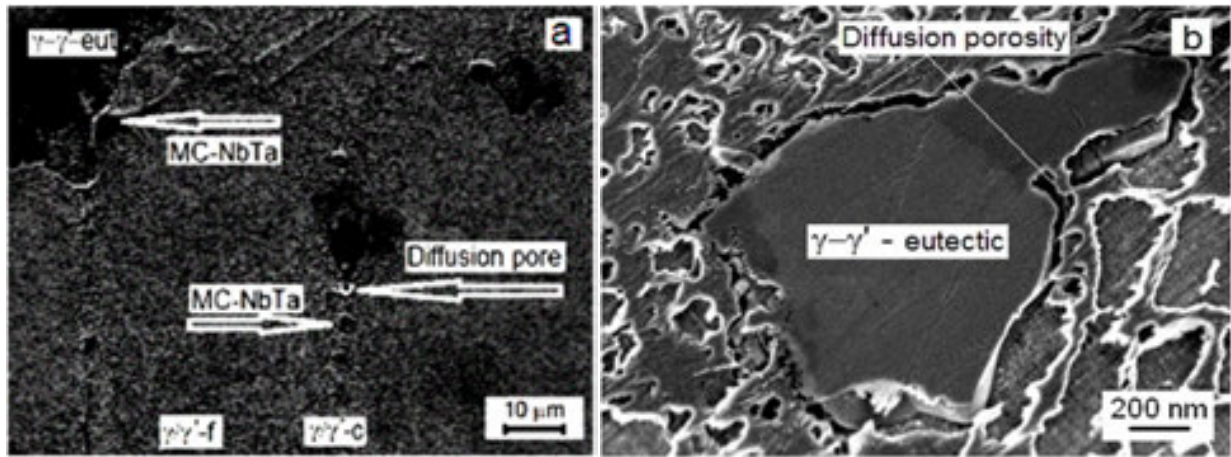

Figure 30. Diffusion micropore (a) and phase/grain boundaries (b) forming in SC as a result of the absence of balanced interdiffusion during HCV deformation.

Such elemental motions change the chemical composition and micromechanical properties of the phases. At an increased cumulative strain and with the absence of balanced interdiffusion, the formation of small pores and phase boundaries (Figure 30) in the interdendritic region of the SC superalloy can be induced. Such defects form as a result of the high diffusion rate for Al in the Ni-based solid solution [47-49].

4.5. SEM/EDS and XRD analysis of microstructure

The atom interdiffusion between the different phases, which changes their elemental concentration based on the cumulative strain increase. The elemental presence for the γ/γ'-phase (a), γ-γ' eutectic phase (b), MC phase (c), and Nb/Ta content in MC phase (d) are also illustrated in Figure 31. The changes of elemental content in the phases during HCV deformation have also been previously described (see Figure 28). The coarse and fine γ/γ'-phases (Figure 31a) contain these same elements but in different concentrations (compare a and b graphs in Figure 28). The eutectic phase pools elemental concentration differed when compared with the γ/γ'-phase. The W and Re contents were lowered. The Nb/Ta-rich MC phases (Figure 31c) also contain W and very small amounts of Ni. A detailed investigation of elemental content in the MC phases show that the Cr, Nb, and Ta concentrations differ (Figure 28) and depend on the cumulative strain and location for the MC phase in the SC region (Figure 31c). The measured nanohardness is high (see Figure 22b) in MC phase near eutectic pools and in the MC phase in the coarse γ/γ'-phase. The PDA and SDA regions don't contain MC phase.

The X-ray investigations (Figure 32) of the initial SC superalloy (S1) showed only one large reflection at 74° on the 2-theta scale and a smaller reflection at 117.7° (d = 0.899; not shown) on the 2-theta scale. These results indicate that the material has a single crystalline microstructure with no grain boundaries or structural defects. The reflection at 74° on the 2-theta scale was significantly decreased at a very low increase of strain-stress influence on the microstructure in the SC sample (S2). Increasing the stress amplitude of the sample (S3) allowed X-ray reflection to occur at 50.6° in the 2-theta scale along with smaller reflections from the tantalum carbide (TaC) compound at lower 2-theta values. Increasing the strain-stress loading formed new peaks and increased the intensity at 50.6° (d = 1.797). The XRD shows that Ni3AlC, Mo0.57Re0.43, and W0.15Ni0.85 formed at the maximum stress-strain loading (S4). The XRD

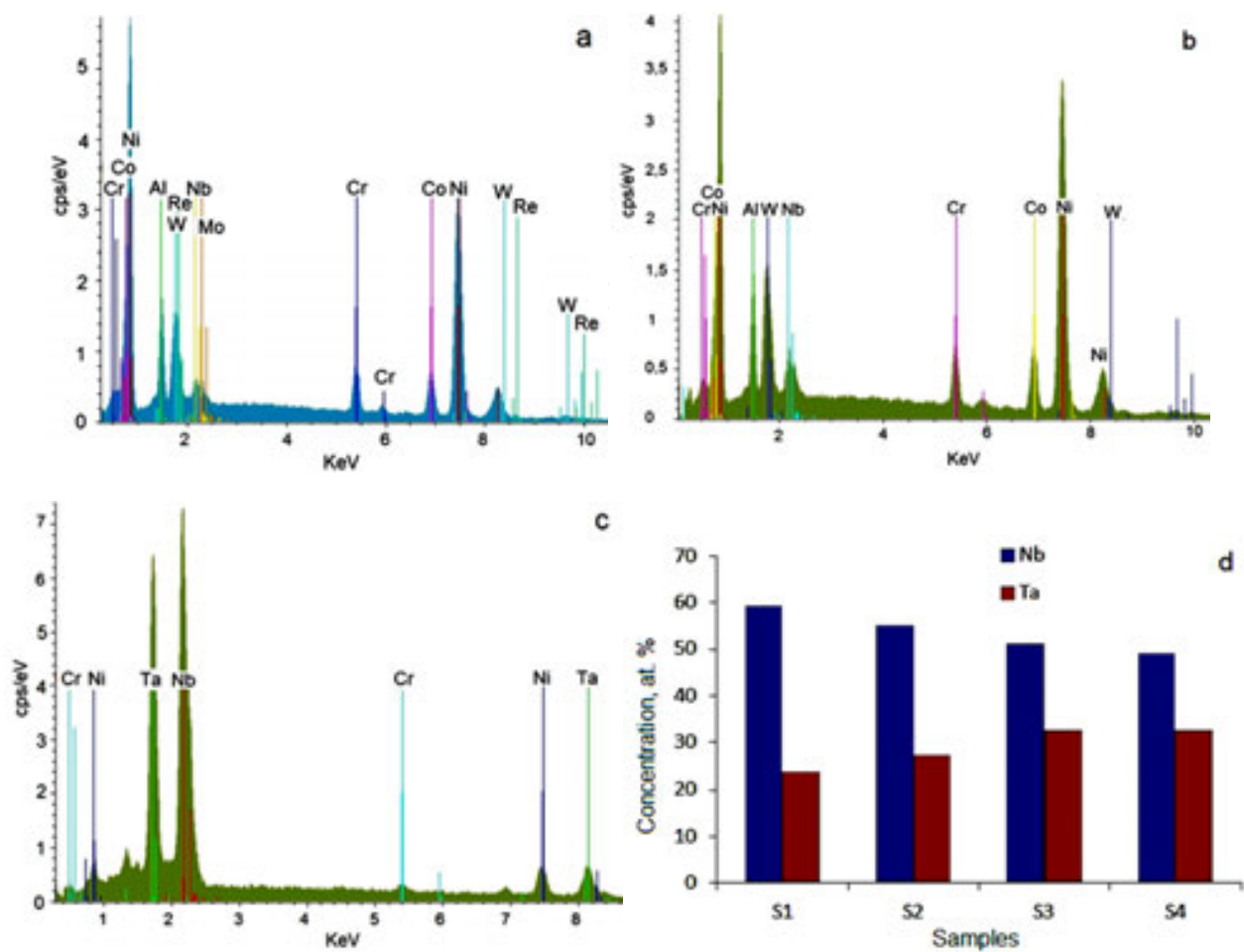**Figure 31.** SEM-EDS diagrams of the sample (S4) in the primary dendrite axis or fine γ/γ′-phase (a), in the eutectic γ-γ′-phase region (b), in the MC phase (c), and Nb/Ta content evolution at interdiffusion in the MC phase (d) of samples.

peaks of the formation of a new proof of the formation of microstructural defects such as pores and grain bound ... ...pores and phase boundaries) were ... ...cture becomes to material with pol ...

4.6. Microstructu ...

Results of the diff ... ...deformation of the SC Ni-based supe ... ...echanism changes (compare with as ... ...ndritic region, the γ-γ′-eutectic pha ... ...metallic γ′-phase had a plaid microstructure (Figure 33b), which was driven symmetrically to tensile compres-

Figure 32. X-ray diffraction diagrams of samples S1, S2, S3, and S4 for different cumulative strains. Adapted from reference [3].
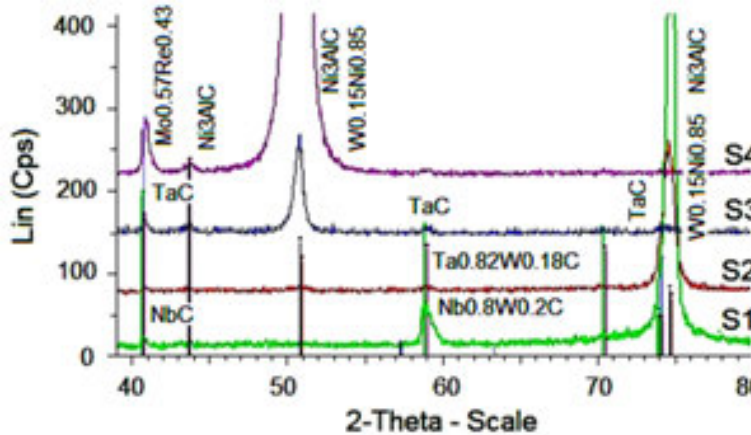
sion loads. The MC carbide phase was mainly rifled in the same direction as the lines. The development of rafted structures strongly influences the mobility of the dislocations and twins [44] and then the rate of strain accumulation especially at relatively low applied stress amplitudes. Deformation

The X-ray investigations (Figure 32) of the initial SC superalloy (S1) showed only one large reflection at 74° on the 2-theta scale and a smaller reflection at 117.7° (*d* = 0.899; not shown) on the 2-theta scale. These results indicate that the material has a single crystalline microstructure with no grain boundaries or structural defects. The reflection at 74° on the 2-theta scale was significantly decreased at a very low increase of strain-stress influence on the microstructure in the SC sample (S2). Increasing the stress amplitude of the sample (S3) allowed X-ray reflection to occur at 50.6° in the 2-theta scale along with smaller reflections from the tantalum carbide (TaC) compound at lower 2-theta values. Increasing the
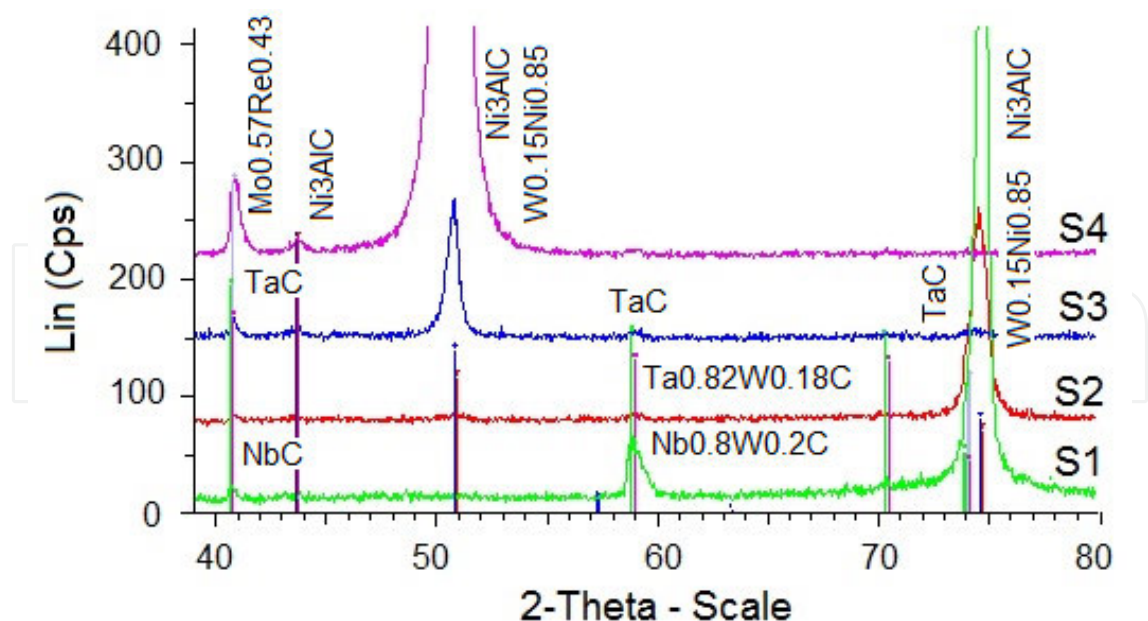
Figure 32. X-ray diffraction diagrams of samples S1, S2, S3, and S4 for different cumulative strains. Adapted from reference [3].

twinning and twinning-related fracture [44] in nickel-based single-crystal superalloys during HCV deformation (Figure 34a) and during thermomechanical fatigue cycling in [6, 7, 51] was studied (Figure 34b). During HCV deformation, a small number of rafts and twins were formed before fracture (Figure 34, a). Such deformation twinning and its related fracture during TMF cycling of Ni-based SC superalloys was studied previously by Zhang et al. [7, 51]. The fracture crack lies by twins formed during TMF cycling (Figure 34b). Analysis of fractured surfaces (after HCV deformation) of tensile specimens show that PDA in the center (Figure 35a) is one of the principal sites for crack initiation in (001) direction, as illustrated in Figure 35b. It is well known that in samples of plastic metals at tension, necking take place with diameter (or cross-section) decrease. In HCV-deformed and tension-fractured samples, necking occurs for each primary dendrite in the core center in the direction of (001). The large number of such longitudinal cracks were formed in fracture surfaces. As a result of interdiffusion, the center part of the dendrite core of PDA has a lowered concentration of Ni and high concentration of Al, and the material has a brittle nature. We believe that such observations have not been shown before. The fracture crack at tension was formed by γ/γ′-phase and by γ-γ′-eutectic phase in the interdendritic region of SC (Figure 36a and b, respectively). As is shown in Figure 36a, the square γ-phase channels were rounded at fracture of the prefatigued SC superalloy. The crack lies mainly by interdendritic zone of secondary dendrites (Figure 37).

As was shown before [10, 11] the damage and fracture of SC Ni-based superalloys are main-ly studied by high cycle fatigue testing at elevated temperatures. For testing, smooth and matched specimens are used. In our studies [3, 28] we show that the damage and fracture depend on phases' chemical content as well phases' micromechanical property changes during testing.

The fracture crack lies by twins formed during TMF cycling (Figure 34b). Analysis of fractured surfaces (after HCV deformation) of tensile specimens show that PDA and the center (Figure 35a) is one of the principal sites for crack initiation in (001) direction, as illustrate in Figure 35b. It is well known that in samples of plastic metals at tension, necking take place with diameter (or cross-section) decrease. In HCV deformed and tension-fractured samples, necking occurs for each primary dendrite in the core center, in the direction of (001). The large number of such longitudinal cracks were formed in fracture surfaces. As a result of interdiffusion, the center part of the dendrite core of PDA has a lowered concentration of Ni and high concentration of Al, and the material has a brittle nature. We believe that such observations have not been shown before. The fracture crack at tension was formed by γ/γ′-phase and by γ-γ′-eutectic phase in the interdendritic region of SC (Figure 36a and b, respectively). As is shown in Figure 36a, the square γ-phase channels were rounded at fracture of the prefatigued SC superalloy. The crack lies mainly by interdendritic zone of secondary dendrites (Figure 37).

Figure 33. Microstructure of interdendritic zone (a) and plaid microstructure of a single γ′-phase (b) after HCV deformation.
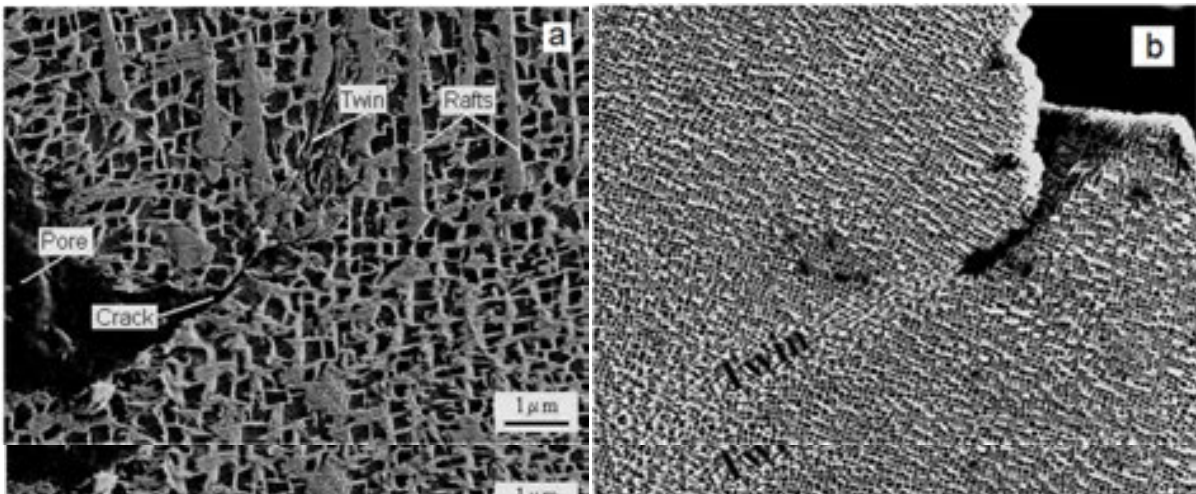

Figure 34. Rafts and twins forming during HCV deformation (a) and deformation twinning and its related fracture during TMF cycling of four nickel-based single-crystal superalloys (b). Adapted from references [28, 51].
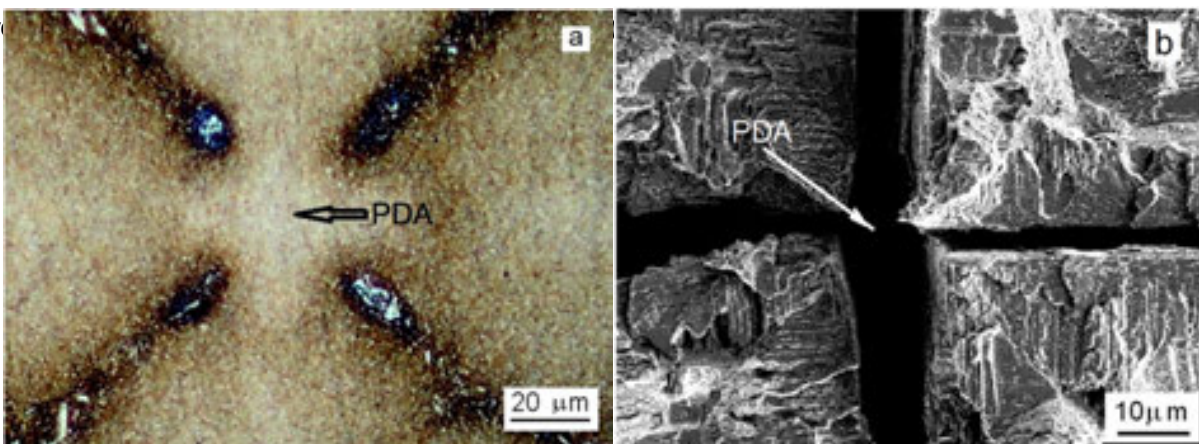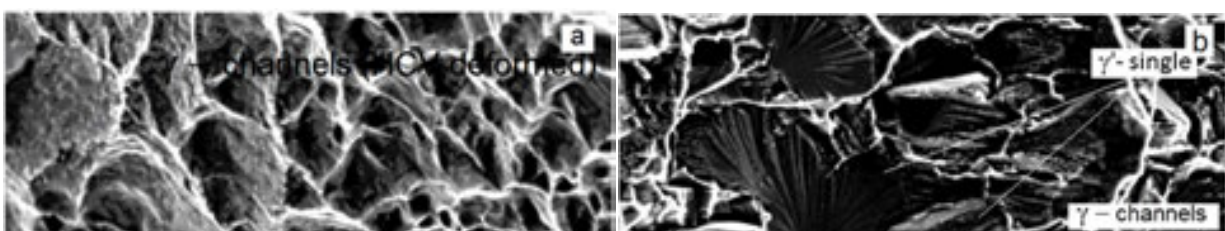

Figure 35. PDA in cross-section (a) and fracture of a preliminarily HCV deformed SC by PDA in (001) direction. Adapted from reference [28]

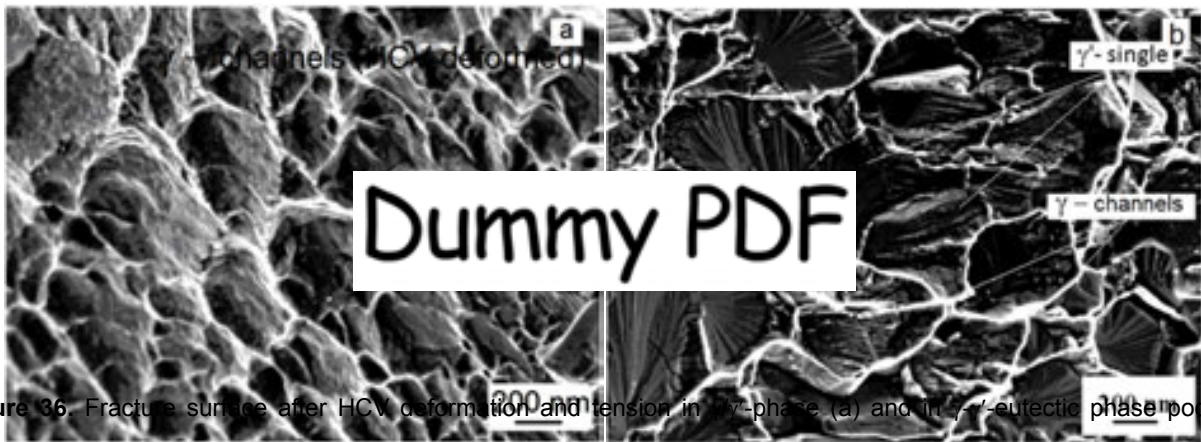**Figure 36.** Fracture surface after HCV deformation and tension in γ/γ'-phase (a) and in γ-γ'-eutectic phase pool (b). Adapted from reference [28]
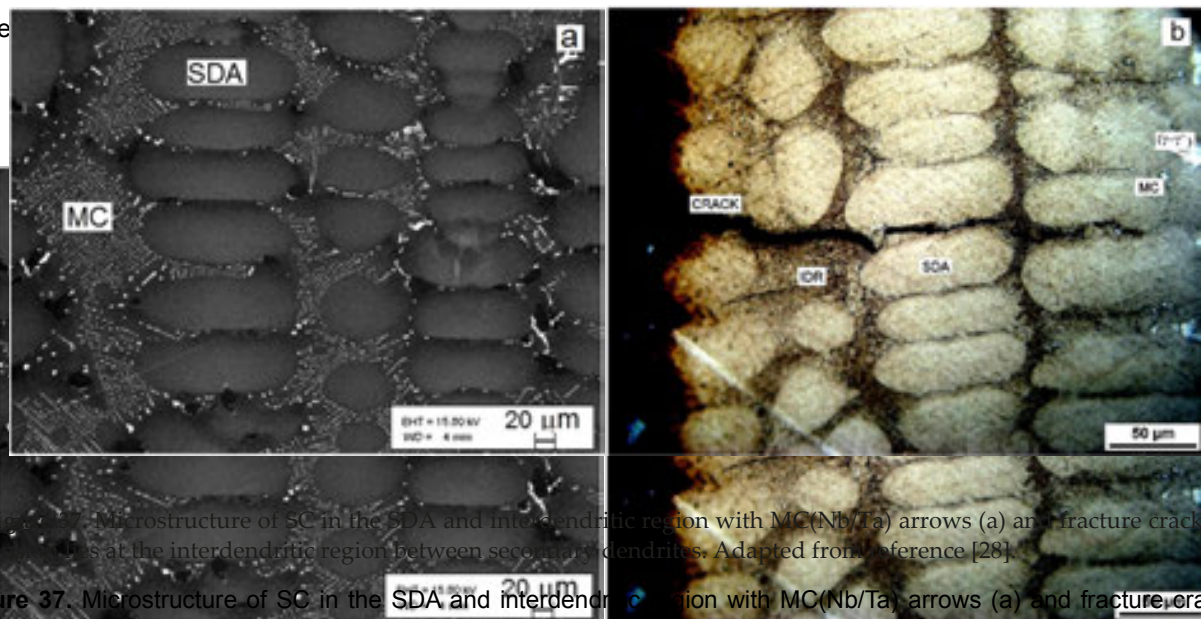

Figure 37. Microstructure of SC in the SDA and interdendritic region with MC(Nb/Ta) arrows (a) and fracture crack at tension lies at the interdendritic region between secondary dendrites. Adapted from reference [28].

5. Conclusions and summary

As was shown before [10, 11] the damage and fracture of SC Ni-based superalloys are mainly studied by high cycle fatigue testing at elevated temperatures. For testing, smooth and matched specimens are used. In our studies [3, 28] we show that the damage and fracture depend on phases' chemical content as well phases' micromechanical property changes during testing.

In this chapter, the phase's equilibrium evolution in single-crystal nickel-based superalloys via chemical condition and micromechanical property changes during hard cyclic viscoplastic deformation at room temperature is presented as a new material characterization method. The samples' microstructure changes at creep testing, as well as damage and fracture mechanisms for different testing modes, are presented. The experimental observation methods—optical microscopy, scanning electron microscopy, transmission electron microscopy, energy-dispersive spectroscopy, microchemical analyses, X-ray diffraction, hard cyclic viscoplastic deformation, and nanoindentation—were combined to obtain new insights into the phase's chemical composition and micromechanical property characterization. Based on the analysis of experimental results and observations, conclusions could be given as follows:

1. The as-cast microstructure of single-crystal nickel-based superalloys, which contain coarse dendrites in the (001) direction with length up to 4.5 mm, were separated by ($\gamma + \gamma'$)-eutectic pools, which significantly reduced

1. The as-cast microstructure of single-crystal nickel-based superalloys, which contain coarse dendrites in the (001) direction with length up to 4.5 mm, were separated by (γ + γ')-eutectic pools, which significantly reduced the length of the newly formed fine dendrites and, as a result, superalloys with a fine microstructure were formed.

2. The area and number of (γ + γ')-eutectic pools in superalloys increased by more than twofold.

3. The interdiffusion of alloyed elements and atoms among the phases changed their micromechanical properties by changing their chemical compositions.

4. These changes differed by elements and depend on the activation energy of elemental diffusion during HCV deformation.

5. At increased strain amplitudes and number of cycles, the SC superalloy softened, and very small diffusion micropores formed in the interdendritic region.

6. The fracture at tension of damaged materials takes place in the interdendritic region and necking by primary dendrites.

7. The results of this investigation provide realistic information concerning shifts in the phase's equilibria evolution and on the changes in the micromechanical properties of phases in SC Ni-based superalloys.

8. Such changes in the phase equilibrium in the SC Ni-based superalloys were influenced by atomic interdiffusion between different neighbor phases by diffusion paths.

We propose that such an investigation can provide realistic information concerning the shifts in phase equilibria of SC Ni-based superalloys, their viability evolution and properties change as well as their fracture mechanisms at increased cumulative strain during HCV deformation. We believe that some results in this chapter have not been reported before.

Acknowledgements

Author details

Lembit Kommel

Address all correspondence to: lembit.kommel@ttu.ee

Tallinn University of Technology, MTI, Tallinn, Estonia

References

[1] Reed RC. The Superalloys: Fundamentals and Applications. New York: Cambridge University Press; 2006.

[2] Wang XG, Liu JL, Jin T. Sun XF. Tensile behaviors and deformation mechanism of a nickel-base single crystal superalloy at different temperatures. Materials Science and Engineering A 2014; 598 154–161.

[3] Kommel L, Kimmari E, Viljus M, Traksmaa R, Volobueva O, Kommel I. Phases micromechanical properties of Ni-base superalloy measured by nanoindentation. Materials Science (Medžiagotyra) 2012; 18(1) 28–33.

[4] Tang H, Cao D, Yao H, Xie M, Duan R. Fretting failure of an aero engine turbine blade. Engineering Failure Analysis 2009; 16 2004–2008.

[5] Sakamoto M, Harada H, Yokokawa T, Koizumi Y, Kobayashi T, Zhou H, Zhang JX, Miyamoto N. Assessment on the thermo-mechanical fatigue properties of 98 Ni-base single crystal superalloys, In: Reed RC, Green KA, Caron P, Gabb TP, Fahrmann MG, Huron ES, Woodard SA (eds.) Superalloys 2008, TMS (The Minerals, Metals & Materials Society) 2008, 521–526.

[6] Zhang JX, Harada H, Ro Y, Koizumi Y, Kobayashi T. Thermomechanical fatigue mechanism in a modern single crystal nickel base superalloy TMS-82. Acta Materialia 2008; 56(13) 2975–2987.

[7] Zhang JX, Harada H, Koizumi Y, Kobayashi T. Crack appearance of single-crystal nickel-base superalloys after thermomechanical fatigue failure. Scripta Materialia 2009; 61 1105–1108.

[8] Moverare JJ, Johansson S, Reed RC. Deformation and damage mechanism during thermal-mechanical fatigue of a single-crystal superalloy. Acta Materialia 2009; 57 2266–2276.

[9] Zhou H, Ro Y, Harada H, Aoki Y, Arai M. Deformation microstructures after low-cycle fatigue in a fourth-generation Ni-base SC superalloy TMS-138. Materials Science and Engineering A 2004; 381 20–27.

[10] Lukáš P, Kunz L, Svoboda M. High cycle fatigue of superalloy single crystals at high mean stress. Materials Science and Engineering A 2004; 387–389 505–510.

[11] Liu Y, Yu JJ, Xu Y, Sun XF, Guan HR, Hu ZQ. High cycle fatigue behavior of a single crystal superalloy. Materials Science and Engineering A 2007; 454–455 357–366.

[12] Akhtar A, Hegde S, Reed RC. The oxidation of single-crystal nickel-based superalloys. JOM 2006; 58(1) 37–42.

[13] Kawagishi K, Harada H, Sato A, Sato A, Kobayashi T. The oxidation properties of fourth generation single-crystal nickel-based superalloy. JOM 2006; 58(1): 43–46.

[14] Epishin A, Link T, Brückner U, Portella PD. Kinetics of the topological inversion of the γ/γ'-microstructure during creep of a nickel-based superalloy. Acta Materialia 2001; 49 4017–4023.

[15] Cormier J, Cailletaud G. Constitutive modeling of the creep behavior of single crystal superalloys under non-isothermal conditions inducing phase transformation. Materials Science and Engineering A 2010; 527 6300–6312.

[16] Chatterjee D, Hazari N, Das N, Mitra R. Microstructure and creep behavior of DMS4-type nickel based superalloy single crystals with orientations near (001) and (011). Materials Science and Engineering A 2010; 528 604–613.

[17] Pierce CJ, Palazotto AN, Rosenberger AH. Creep and fatigue interaction in the PWA1484 single crystal nickel-base alloy. Materials Science and Engineering A 2010; 527 7484–7489.

[18] Cutler ER, Wasson AJ, Fuchs, GE. Effect of minor alloying additions on the solidification of single-crystal Ni-base superalloy. Journal of Crystal Growth 2009; 311 3753–3760.

[19] Zeng Q, Ma SW, Zheng YR, Liu SZ, Zhai T. A study of Re and Al diffusion in Ni. Journal of Alloys and Compounds 2009; 480 987–990.

[20] Wilson BC, Cutler ER, Fuchs GE. Effect of solidification parameters on the microstructures and properties of CMSX-10. Materials Science and Engineering A 2008; 479 356–364.

[21] Kim SH, Kim JM, Lee HJ, Son SD, Lee JH, Seo SM, Jo CY. Effect of thermal gradient on solidification microstructure in the Ni-base single crystal superalloy CMSX10. Defect and Diffusion Forum 2008; 273–276 361–366.

[22] Liu L, Hang T, Zou M, Zhang W, Zhang J, Fu H. The effects of withdrawal and melt overheating histories on the microstructure of a nickel-based single crystal superalloy. In: Roger CR, Green KA, Caron P, Gabb TP, Fahrmann MG, Huron ES, Woodard SA. (Eds.) TMS Superalloys-2008 287–293.

[23] El-Bagoury N, Nofal A. Microstructure of an experimental Ni base superalloy under various casting conditions. Materials Science and Engineering A 2010; 527 7793–7800.

[24] Reed RC, Cox DC, Rae CMF. Damage accumulation during creep deformation of a single crystal superalloy at 1150°C. Materials Science and Engineering A 2007; 448(1–2) 88–96.

[25] Ugaste Ű, Priimets J, Laas T. Dependence of diffusion paths on thermodynamic factors in ternary systems. Defect and Diffusion Forum 2008; 277 119–124. DOI: 10.4028/www.scientific.net/DDF.277.119.

[26] Gebura M, Lapin J. Microsegregation induced inhomogeneity of coarsening of γ' precipitates in a nickel-based single crystal superalloy. Defect and Diffusion Forum 2010; 297–301 826–831. DOI:10.4028/www.scientific.net/DDF.297-301.826.

[27] Tiwari GP, Mehrotra RS. Diffusion and melting. Defect and Diffusion Forum 2008; 279 23–37. DOI:10.4028/www.scientific.net/DDF.279.23.

[28] Kommel LA, Straumal BB. Diffusion in SC Ni-base superalloy under viscoplastic deformation. Defect and Diffusion Forum 2010; 297–301 1340–1345. DOI:10.4028/www.scientific.net/DDF.297–301.1340.

[29] Liu LR, Jin T, Zhao NR, Sun XF, Guan HR, Hu ZQ. Formation of carbides and their effects on stress rupture of a Ni-base single crystal superalloy. Materials Science and Engineering A 2003; 361 191–197.

[30] Zhang J, Li B, Zou M, Wang C, Liu L, Fu H. Microstructure and stress rupture property of Ni-based monocrystal superalloy with melt superheating treatment. Journal of Alloys and Compounds 2009; 484 753–756.

[31] Mughrabi H. Microstructural aspects of high temperature deformation of monocrystalline nickel base superalloys: some open problems. Materials Science and Technology 2009; 25(2) 191–204.

[32] Graverend J-B, Cormier J, Jouiad M, Gallerneau F, Paulmier P, Hamon F. Effect of fine γ' precipitation on non-isothermal creep and creep-fatigue behavior of nickel base superalloy MC2. Materials Science and Engineering A 2010; 527 5295–5302.

[33] Rae CMF, Reed RC. Primary creep in single crystal superalloys: Origins, mechanisms and effects. Acta Materialia 2007; 55 1067–1081.

[34] Huda Z. Metallurgical failure analysis for a blade failed in a gas-turbine engine of a power plant. Materials and Design 2009; 30 3121–3125.

[35] Brückner U, Epishin A, Link T, Fedelich B, Portella PD. Dendritic stresses in nickel-base superalloy. Materials Science Forum 2005; 490–491 497–502.

[36] Huang M, Zhao L, Tong J. Discrete dislocation dynamic modelling of mechanical deformation of nickel-based single crystal superalloys. International Journal of Plasticity 2012; 28 141–158.

[37] Yashiro K, Kurose F, Nakashima Y, Kubo K, Tomita Y, Zbib HM. Discrete dislocation dynamic simulation of cutting of γ' precipitate and interfacial dislocation network in Ni-based superalloy. International Journal of Plasticity 2006; 22 713–723.

[38] Shenoy MM, McDowell DL, Neu RW. Transversely isotropic viscoplasticity model for a directionally solidified Ni-base superalloy. International Journal of Plasticity 2006; 22 2301–2326.

[39] Kommel L. Viscoelastic behavior of a single-crystal nickel–base superalloy. Materials Science (Medžiagotyra) 2009; 15(2) 123-128.

[40] Takagi H, Fujiwara M, Kakehi K. Measuring Young's modulus of Ni-based superalloy single crystals at elevated temperatures through microindentation. Materials Science and Engineering A 2004; 387–389 348–351.

[41] Durst K, Göken M. Micromechanical characterisation of the influence of rhenium on the mechanical properties in nickel-base superalloys. Materials Science and Engineering A 2004; 387–389 312–316.

[42] Schöberl T, Gupta HS, Fratzl P. Measurements of mechanical properties in Ni-base superalloys using nanoindentation and atomic force microscopy. Materials Science and Engineering A 2003; 363 211–220.

[43] Neumeier S, Dinkel M. Pyczak F. Göken M. Nanoindentation and XRD investigations of single crystalline Ni-Ge brazed nickel-base superalloys PWA 1483 and René N5. Materials Science and Engineering A 2011; 528 815–822.

[44] Kommel L. New technique for characterization of microstructure of the nickel-base superalloy. In: Proceedings of the 7th International DAAAM Baltic Conference, Industrial Engineering, 22–24 April 2010, Tallinn, Estonia.

[45] Epishin A, Link T, Klingelhöffer H, Fedelich B, Brückner U, Portella PD. New technique for characterization of microstructural degradation under creep: Application to the nickel–base superalloy CMSX-4. Materials Science and Engineering A 2009; 510–511 262–265.

[46] Kommel L. Effect of hard cyclic viscoplastic deformation on phases chemical composition and micromechanical properties evolution in single crystal Ni-base superalloy. Acta Physica Polonica (In print)

[47] Whitesell HS, Li L, Overfelt RA. Influence of solidification variables on the dendrite arm spacing of Ni-based superalloy. Metallurgical and Materials Transactions 2000; 31B 546–551.

[48] Razumovskii IM, Ruban AV, Razumovskiy VI, Logunov AV, Larionov VN, Ospennikova OG, Poklad VA, Johansson B. New generation of Ni-based superalloys designed on the basis of first-principles calculations. Materials Science and Engineering A 2008; 497 18–24.

[49] Orlov MP. The mechanism of porous forming and viability of monocrystallic turbine blades. Deformation and Fracture of Materials 2008; 6 43–48 (in Russian).

[50] Dirand L, Cormier J, Jacques A, Chateau-Cornu J-P, Schenk T, Ferry O, Bastie P. Measurement of the effective γ/γ' lattice mismatch during high temperature creep of Ni-based single crystal superalloy. Materials Characterization. 2013; 77 32–46.

[51] Sun F, Zhang J, Harada H. Deformation twinning and twinning-related fracture in nickel-base single-crystal superalloys during thermomechanical fatigue cycling. Acta Materialia 2014; 67 45-57.